

IMPERIAL

**ADAPTIVE IQ CANCELLATION LOOP FOR
ARTEFACT SUPPRESSION IN HETERODYNE
ELECTROPHYSIOLOGY**

Author

A. GOTTESMAN

CID: 06016005

Supervised by

DR N. GROSSMAN
PROF. T. CONSTANDINOU

A Thesis submitted in fulfillment of requirements for the degree of
Master of Science in Analogue and Digital Integrated Circuit Design

Department of Electrical and Electronic Engineering
Imperial College London
2025

Abstract

An adaptive in-phase/quadrature (I/Q) cancellation loop is introduced to suppress stimulation artefacts that currently limit the ability to prove non-invasive heterodyne electrophysiology during kHz stimulation. The vector-locked, lock-in architecture confines energy with a carrier-centred band-pass, performs coherent I/Q demodulation, applies digital low-pass smoothing with residual-weighted LMS adaptation, and remodulates a synchronised anti-signal for subtraction. Analogue LTspice models characterise control dynamics, and a MATLAB–NI-DAQ realisation achieves substantially deeper, more stable nulls. In vivo at 2 kHz tACS ($\leq 3 \text{ mA}$), the carrier peak is reduced by 82.7 dB. Post-cancellation spectra exhibit low-frequency sidebands ($\sim 0.2\text{--}0.3 \text{ Hz}$ and $\sim 1\text{--}1.3 \text{ Hz}$ with harmonics) consistent with physiological modulation that presently mask any putative heterodyned neural signals. In a two-tone TI experiment (2 kHz, 2.01 kHz), coherently nulling a single carrier eliminates the 10 Hz difference-frequency artefact, indicating promising utility for artefact-minimised TI-EEG. Next steps bifurcate: on-head cancellation with external phase locking for artefact-free EEG recording during TI brain stimulation, and localisation of the physiological sidebands' origin within the signal chain to enable a reliable non-invasive assessment of neural heterodyning.

Contents

Acknowledgements	iv
1 Introduction	1
2 Background	2
2.1 Motivation	2
2.2 Evidence	3
2.3 Proposal	6
2.4 Obstacles	6
3 Stimulation Artefact Analysis	9
3.1 The Challenge	9
3.2 Naïve Solutions	9
3.3 Modelling the Artefact	10
4 Method	16
4.1 Control System Model	16
4.2 Signal Processing Model	16
4.3 Physical Model	17
5 Analogue Simulation	19
5.1 Circuit Building Blocks	19
5.2 Schematic	19
5.2.1 Closed-Loop Path	19
5.2.2 Limits of Closed-Loop Path	21
5.2.3 Open-Loop Path	24
5.3 Redundant Complexity	24
5.4 Performance	24
6 Digital Implementation	29
6.1 Overview	29
6.2 Performance	31
7 Experimentation	32
7.1 Instrumental IMD Test	32
7.2 In Vivo Setup	33
7.3 Eyes Open vs. Eyes Closed Test	34
7.4 Pre- vs. Post-Cancellation	34

7.5	NI DAQ Update Clicks	35
7.6	Profiles of Post-Cancellation Recordings	36
8	Further Applications	39
8.1	TI In Vivo Setup	39
8.2	Performance	40
9	Discussion	42
9.1	Integrative Summary	42
9.2	Further Conclusions	43
9.3	Novelty and Positioning	44
9.4	Limitations and Future Directions	44
10	Sustainability and Societal Impact	45
10.1	Environmental footprint and sustainability	45
10.2	Societal benefits and opportunities	45
10.3	Risks, ethics, and mitigations	45
10.4	Future sustainability actions	45
11	Conclusion	46
A	Adaptive Cancellation Script	49

Acknowledgements

I am grateful to my supervisor, Dr Nir Grossman, and my mentor, Assaf Touboul, for equipping me with the intellectual and practical tools to tackle the challenges of this work. They took a genuine interest in each incremental development and consistently directed my attention to the most critical issues. I am thankful to Thomas Deegan and Dr Edward Rhodes for their help in setting up the experiments; meaningful conclusions would not have been possible without their support. I also acknowledge the technical assistance of Dr Jonathan Howard, which was crucial for getting the instrumentation operational. Finally, I appreciate all members of the Interventional Systems Neuroscience (ISN) group for creating a stimulating interdisciplinary environment.

1 Introduction

Non-invasive heterodyne electrophysiology faces a practical barrier: a dominant stimulation artefact can obscure relevant spectral content near the drive frequency. A cancellation strategy is therefore required to suppress the artefact while preserving spectral components close to the carrier. This matters in kHz stimulation paradigms, where physiological information is hypothesised to appear in sidebands near the carrier via nonlinear mixing.

This report develops and studies such a strategy. It begins with the Background section, which summarises the clinical motivation and the hypothesis that endogenous rhythms can be shifted onto a high-frequency carrier. The Stimulation Artefact Analysis section then explains why naïve fixes fall short and distils requirements for an effective approach. Building on these, the Method section sets out the conceptual framework that guides design. Analogue Simulation explores loop behaviour and circuit-level trade-offs, while Digital Implementation presents a software realisation suitable for practical use. Experimentation describes the human recording setup and evaluation procedures under transcranial stimulation. Finally, Further Applications sketches additional use cases, and the Discussion synthesises findings, positions novelty, and outlines limitations with future directions.

2 Background

This section introduces the motivation and hypothesis for non-invasive neural heterodyning, delineates an ambitious scheme, and highlights the principal obstacles to feasibility.

2.1 Motivation

Deep Brain Stimulation (DBS) has become a cornerstone therapy for severe, drug-refractory motor symptoms in Parkinson's disease (PD) [1]. While invasive DBS provides effective and precise modulation of deep neural circuits, it carries risks of surgical complications, hardware failure, and long-term management burdens [2]. These drawbacks have prompted interest in non-invasive brain stimulation (NIBS) approaches, such as Temporal Interference (TI).

TI uses two electric fields (typically kHz-range) to generate a low-frequency envelope that can reach deep brain regions [3]. Compared with conventional transcranial methods, TI offers better spatial focus [4] but remains less precise than invasive DBS for targets such as the subthalamic nucleus (STN), globus pallidus interna (GPi), and globus pallidus externa (GPe) [5] [6]. Clinical application also requires a non-invasive readout of deep targets, typically via electroencephalography (EEG). However, EEG primarily measures superficial cortical signals and rarely captures activity from structures such as the STN and GPi [7]. These constraints motivate research into non-invasive recording of deep neural activity.

In this context, an interdisciplinary perspective that bridges neuroscience and telecommunications through frequency mixing has been set out by Assaf Touboul (AT), the author's mentor and a PhD student supervised by Dr. Nir Grossman and Dr. Shlomi Haar at Imperial College London. It builds on the biophysical observation that neurons can mix multiple exogenous electric field inputs, producing oscillatory components at the sum and difference of the input frequencies (see Figure 1) [8]. The mechanism is analogous to a diode (a non-linear semiconductor device), which mixes frequencies owing to its exponential voltage–current relationship [9]; this non-linear mixing behaviour is used extensively in radio-frequency (RF) technology, including mixer and detector circuits [10]. In TI, such mixing allows neurons to respond to the low-frequency envelope generated by two high-frequency inputs [3].

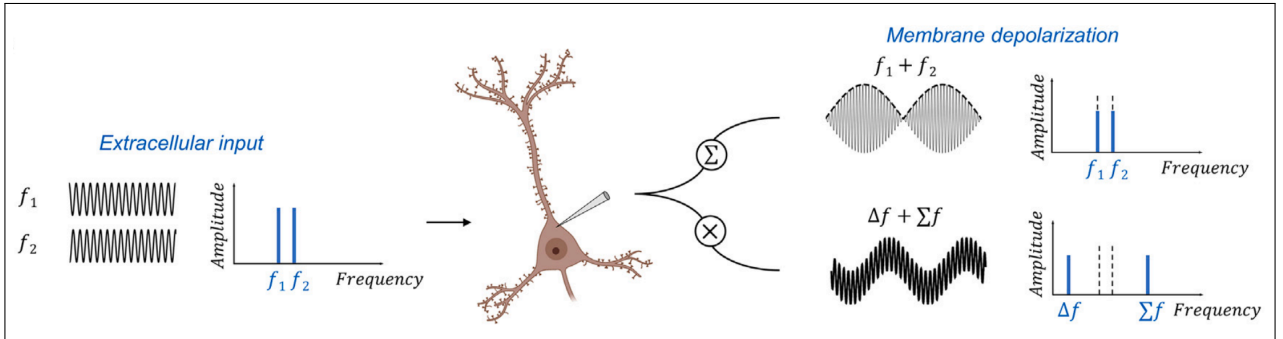


Figure 1: The neural mixing concept illustrates the subthreshold membrane transfer function of multi-frequency input, contrasting conventional linear superposition (Σ) with the proposed nonlinear mixing via multiplication (\times) (taken from [8]).

This observation raises a fundamental question: can neurons act as biological mixers that shift endogenous neural activity onto an externally applied high-frequency carrier signal? If so, stimulation parameters could be used to modulate deep neural activity at chosen frequencies. However, such carrier-based modulation of endogenous activity has not yet been experimentally validated. In other words, although the main TI mechanism posits that two exogenous electric fields interact in the extracellular space and are modulated via neuronal mixing, there is currently no canonical evidence that exogenously applied electric fields can amplitude-modulate endogenous neural activity.

2.2 Evidence

To evaluate empirical support for carrier-based modulation of endogenous activity, *in vivo* suprathreshold local field potential (LFP) responses from the STN of patients with PD during DBS were analysed by AT. A publicly available dataset [11] comprising 27 participants with idiopathic PD was used. In total, the cohort covered 36 hemispheres, with a mean age of 60.42 ± 1.22 years and a mean disease duration of 10.85 ± 0.98 years [12]¹. The dataset includes ON- and OFF-levodopa recordings for 30 hemispheres [12], and provides EEG channels, bipolar LFP channels, and triaxial accelerometer signals [11]. Figure 2 summarises the stimulation protocols used during data collection and the associated spectrograms.

Guided by the hypothesis that neuronal populations during DBS act as non-linear frequency mixers, AT's prediction was that beta oscillations (13–30 Hz), when mixed with a 130 Hz stimulation train, would produce sidebands – spectral power at the 130 Hz harmonics and at harmonic \pm beta offsets – consistent with amplitude modulation (see Figure 3).

Spectral and temporal analyses in Figure 4 and Figure 5 support this prediction. Power spectra show that, beyond the 130 Hz fundamental and its harmonics, sidebands appear at harmonic \pm beta, consistent with heterodyning of endogenous beta oscillations with the exogenous DBS electric field. These sidebands are observed around the first, second, and third harmonics, indicating that pathological beta activity is frequency-shifted onto the DBS carrier. Furthermore, the time-domain analysis in Figure 5 shows that the raw signal, band-pass filtered around the second harmonic (± 40 Hz) and then coherently demodulated, closely tracks spontaneous beta oscillations, with a Pearson correlation of 0.79 and an effect ratio (ER) relative to a control signal of 30.46. Moreover, Figure 6 shows that heterodyned beta activity at DBS harmonics is significantly correlated with endogenous beta (13–30 Hz) across all harmonics: box plots indicate higher correlation coefficients for the demodulated beta signal than for the control, with ERs ranging from 2.30 to 4.97. At the group level, pooling across harmonics yields an ER of 3.25, confirming a robust correlation advantage for the demodulated signal and supporting consistent non-linear frequency mixing between endogenous and exogenous activity.

¹The dataset was originally collected under IRAS 46576 and is hosted by the UKRI Medical Research Council [11].

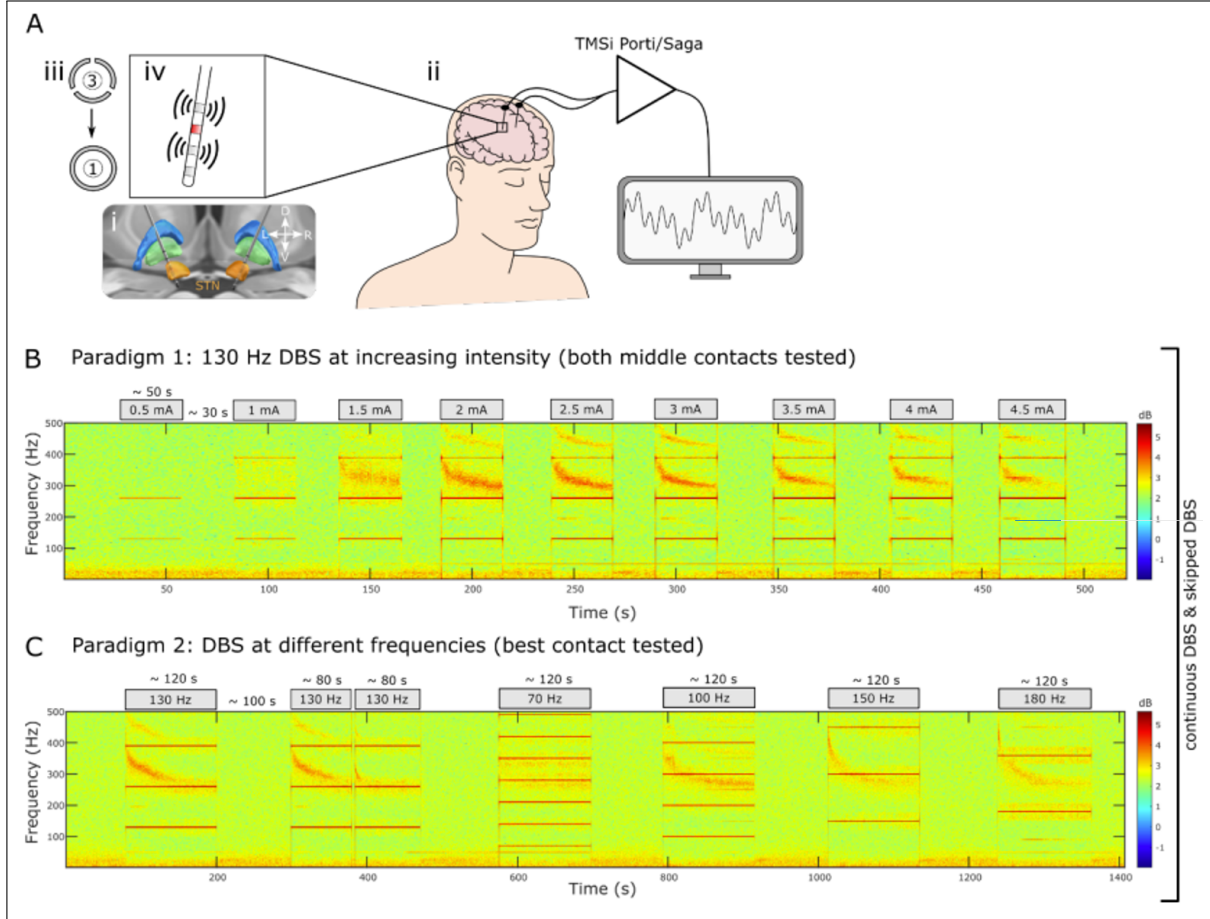


Figure 2: **Experimental setup and stimulation paradigms.** (A) Bilateral STN electrodes were implanted (i) and externalised (ii). Directional contacts were combined into a ring (iii); stimulation was delivered via one middle level (red), with adjacent contacts for bipolar recordings (iv). (B) Spectrogram from the bipolar channel around the stimulation contact (Paradigm 1; patient 6, left hemisphere); DBS intensity stepped by 0.5 mA. (C) The contact level/current maximising evoked resonant neural activity (ERNA) in Paradigm 1 defined the frequency tests in Paradigm 2. Both paradigms used continuous and skipped-DBS (taken from [12]).

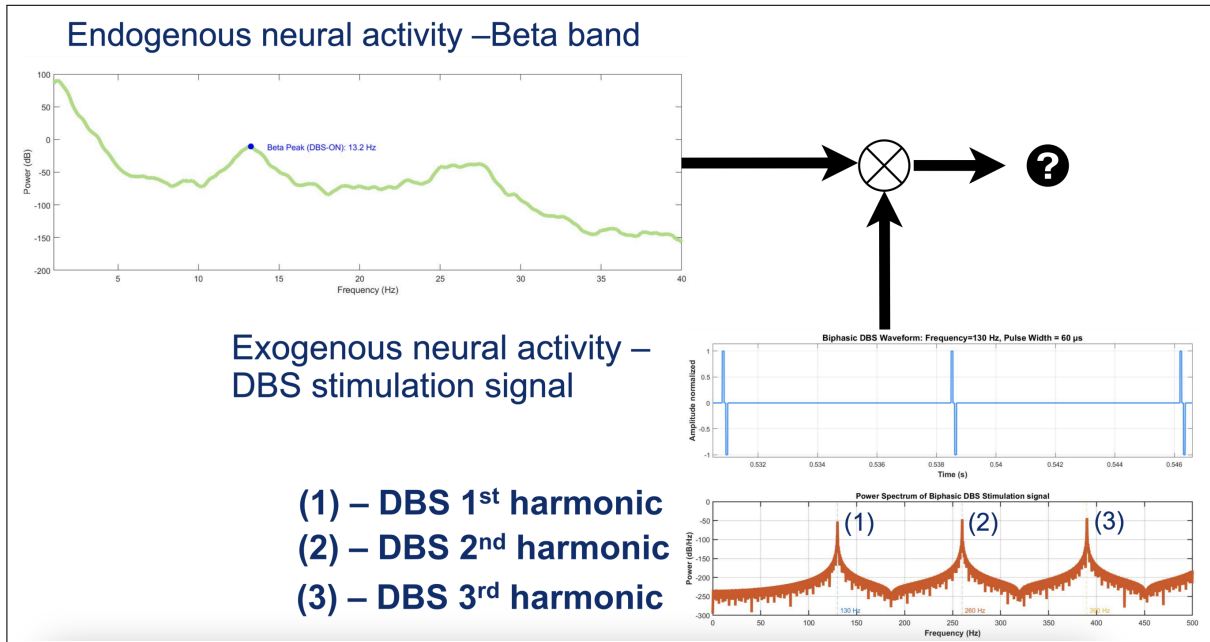


Figure 3: Schematic of hypothesised DBS heterodyning via nonlinear mixing (adapted from AT).

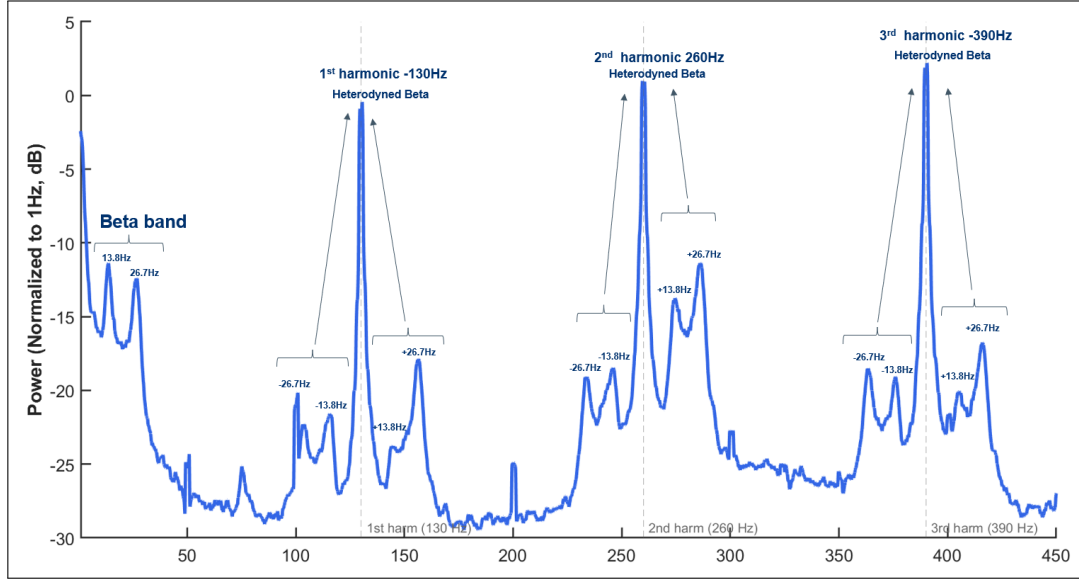


Figure 4: Spectral evidence of nonlinear frequency mixing in STN during DBS (provided by AT).

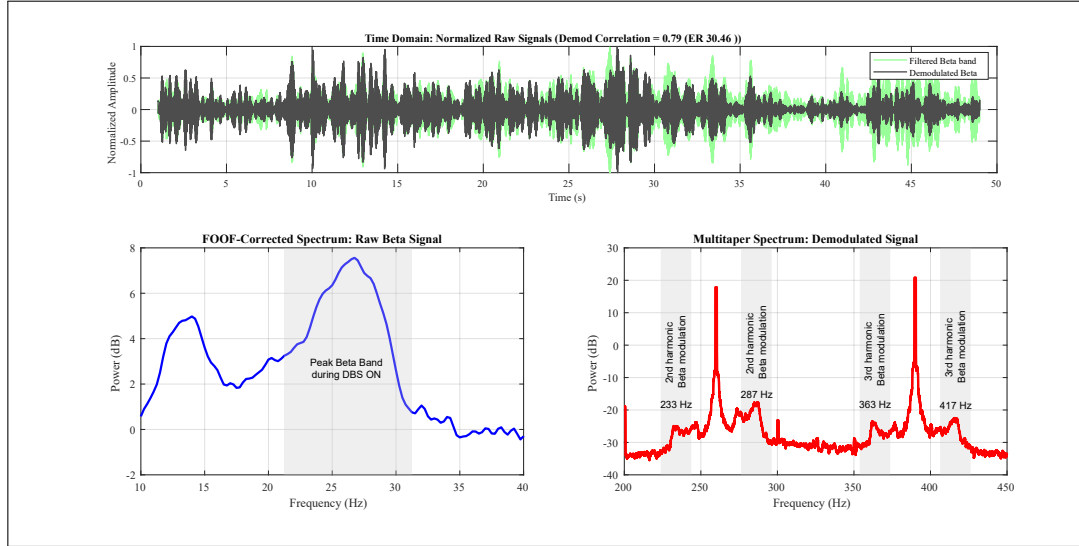


Figure 5: Time-domain evidence of beta modulation in STN during DBS (provided by AT).

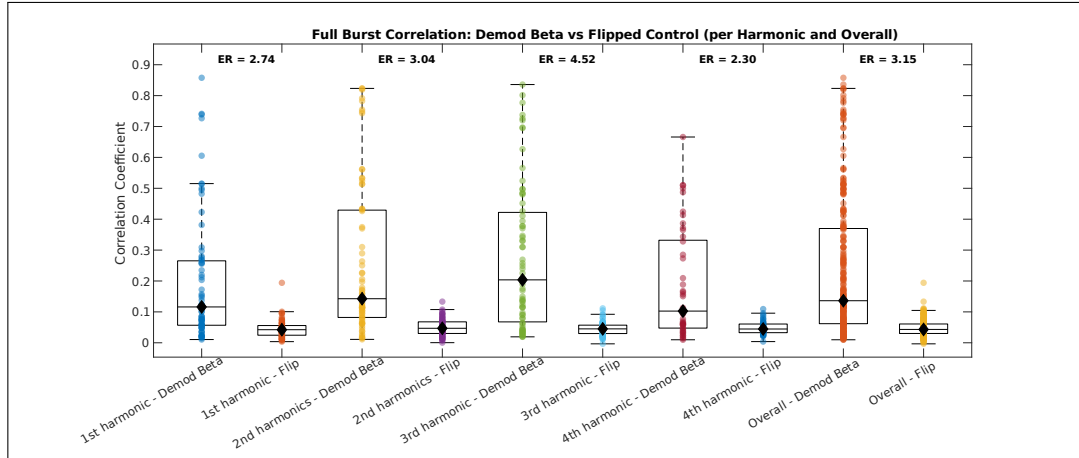


Figure 6: Group-level correlations between demodulated and endogenous beta (provided by AT).

2.3 Proposal

Since spectral evidence in PD indicates that LFPs interact with DBS, an EEG heterodyning approach is proposed by AT and illustrated in Figure 7. In this scheme, deep neural activity is conveyed on high-frequency carriers and recovered at the scalp. To target different depths, multiple carriers (f_1, f_2, f_3) are delivered through isolated electrode pairs (Figure 7A). Each carrier amplitude-modulates the local activity, and EEG records the composite spectrum (Figure 7B). As a result, depth is encoded as frequency-specific amplitude patterns (A_1, A_2, A_3) that can be separated and demodulated to reconstruct activity from distinct spatial locations (Figure 7C–D). This, in turn, enables non-invasive stimulation and recording, with the spatial origin encoded in the frequency domain. Finally, assigning each stimulation site a unique frequency tag permits discrimination of signals from different brain areas, similar to spatial multiplexing. If successful, this neural heterodyning approach could overcome the depth-resolution limitations of conventional EEG, enabling non-invasive, multi-site deep-brain recording and stimulation. It could also support real-time closed-loop neuromodulation and next-generation brain–machine interfaces that are wireless, minimally invasive and scalable.

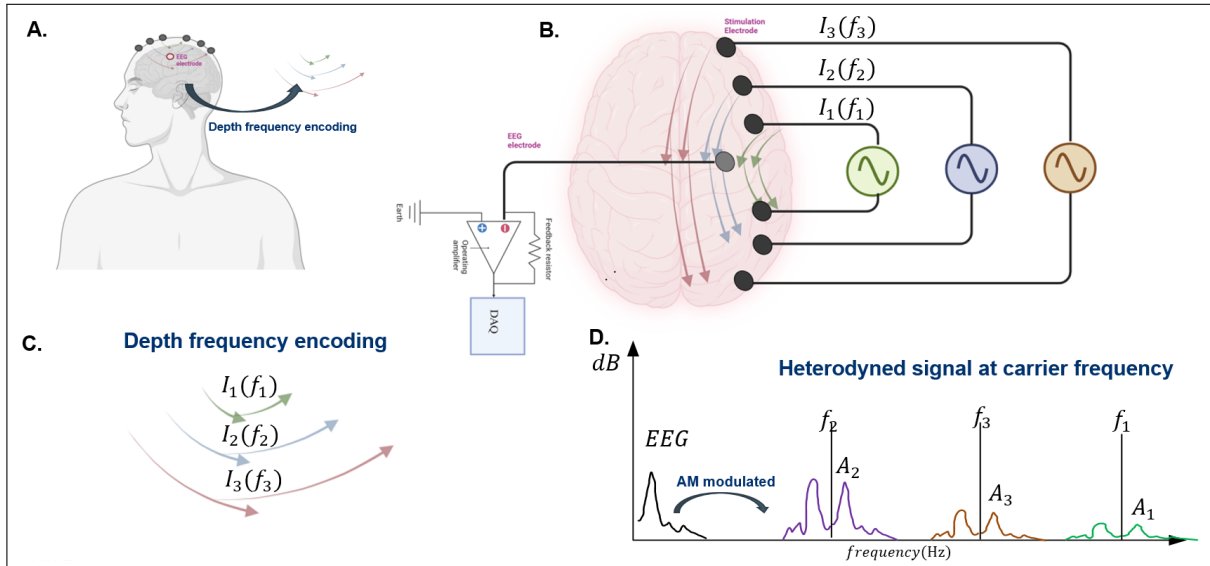


Figure 7: Non-invasive space-to-frequency encoding scheme (provided by AT).

2.4 Obstacles

Translating the above proposal to non-invasive recordings requires evidence of neural heterodyning in EEG; at present, such evidence is lacking. Although heterodyning-like effects are observed in LFPs during DBS, they have not yet been demonstrated at the scalp. The principal obstacle is the stimulation artefact: leakage signals can exceed the neural signal by orders of magnitude (EEG amplitudes are typically in the μV range), and phase noise further masks the underlying activity. This leakage also drives the acquisition chain toward saturation, affecting both the recording amplifier and the analogue-to-digital converter (ADC). A further complication is that hardware non-linearities themselves produce frequency mixing –i.e., inter-modulation distortion (IMD)– generating spectral components which can be mistaken for neural heterodyning. Disentangling biophysical effects from instrumental IMDs therefore calls for specialised cancellation techniques and careful front-end design.

Accordingly, the approach faces three technical challenges: (i) suppressing stimulation artefacts; (ii) recording weak neural signals in the presence of strong interference by managing dynamic range; and (iii) mitigating hardware non-linearities. Addressing (ii) hinges on the analogue front end, in particular the ADC. Its dynamic range, defined as the dB difference between the quantisation-noise floor and the maximum representable input, is governed by the effective number of bits (ENOB) and the oversampling ratio (OSR) [13]. Turning to (iii), the non-linearities in amplifiers and other active circuits can be modelled with a Taylor expansion [14]:

$$y(t) = a_1x(t) + a_2x^2(t) + a_3x^3(t) + \dots \quad (1)$$

With a two-tone input

$$x(t) = A_1 \cos(\omega_1 t) + A_2 \cos(\omega_2 t), \quad (2)$$

where the second- and third-order terms generate inter-modulation (IM) components. Using the identities

$$\cos^2 \theta = \frac{1}{2}(1 + \cos 2\theta), \quad \cos \alpha \cos \beta = \frac{1}{2}[\cos(\alpha - \beta) + \cos(\alpha + \beta)], \quad \cos^3 \theta = \frac{1}{4}(3 \cos \theta + \cos 3\theta),$$

one obtains

$$y_2(t) = a_2x^2(t) = a_2 \left[\frac{A_1^2}{2}(1 + \cos 2\omega_1 t) + \frac{A_2^2}{2}(1 + \cos 2\omega_2 t) + A_1 A_2 (\cos(\omega_1 - \omega_2)t + \cos(\omega_1 + \omega_2)t) \right], \quad (3)$$

$$\begin{aligned} y_3(t) = a_3x^3(t) &= a_3 \left[\frac{3A_1^3}{4} \cos \omega_1 t + \frac{A_1^3}{4} \cos 3\omega_1 t + \frac{3A_2^3}{4} \cos \omega_2 t + \frac{A_2^3}{4} \cos 3\omega_2 t \right. \\ &\quad + \frac{3}{2}A_1^2 A_2 \cos \omega_2 t + \frac{3}{4}A_1^2 A_2 (\cos(2\omega_1 - \omega_2)t + \cos(2\omega_1 + \omega_2)t) \\ &\quad \left. + \frac{3}{2}A_1 A_2^2 \cos \omega_1 t + \frac{3}{4}A_1 A_2^2 (\cos(2\omega_2 - \omega_1)t + \cos(2\omega_2 + \omega_1)t) \right]. \end{aligned} \quad (4)$$

Hence

$$\text{2nd-order IMD: } \omega_1 \pm \omega_2; \quad \text{3rd-order IMD: } 2\omega_1 \pm \omega_2, 2\omega_2 \pm \omega_1,$$

together with harmonics at $2\omega_1, 2\omega_2, 3\omega_1, 3\omega_2$ and small fundamental gain shifts (see Figure 8). In the carrier-plus-beta case, these sum and difference terms coincide with the expected heterodyned sidebands. Consequently, instrumental IMDs must be distinguished from true neural heterodyning to substantiate the latter. However, this discrimination is feasible only after obstacle (i), the stimulation artefact, has been suppressed. The next section addresses this prerequisite.

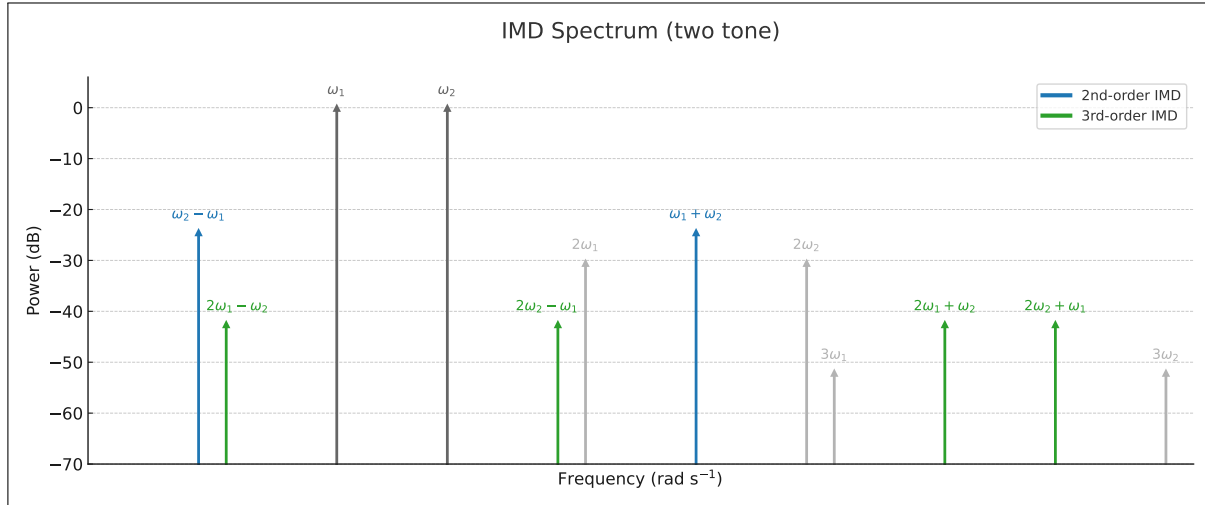


Figure 8: Spectrum showing modelled IMD orders.

Summary

- **Clinical motivation:** DBS is effective but invasive; TI offers a non-invasive route to deep targets using kHz carriers.
- **Core hypothesis:** neuronal non-linearities could mix exogenous fields so endogenous rhythms ride on high-frequency carriers.
- **Evidence so far (invasive):** STN LFPs during DBS show patterns consistent with mixing; no canonical non-invasive demonstration yet.
- **Proposed idea:** space-to-frequency encoding with multiple carriers to tag regions and recover depth-specific activity at the scalp.
- **Main obstacle:** a dominant stimulation artefact that dwarfs cortical signals thus confounding interpretation; hardware non-linearities may also mimic neuronal mixing.
- **Consequence:** establishing feasibility requires understanding and controlling the artefact before testing for neural heterodyning.

3 Stimulation Artefact Analysis

This section addresses obstacle (i): the stimulation artefact. It outlines potential remedies and ultimately develops a model that provides an effective approach.

3.1 The Challenge

As noted in the Background section, canonical evidence of neural heterodyning in EEG during NIBS remains absent. This is due to the stimulation artefact being about five orders of magnitude larger than cortical signals, producing a close-in phase-noise skirt that obscures putative IM sidebands. Figure 9 illustrates the issue: an ideal sinusoid appears as an impulse in the frequency domain, whereas a real oscillator exhibits phase noise that spreads energy into close-in skirts around the carrier [15]. Because these skirts are temporally correlated, unlike white noise, averaging does not eliminate them.

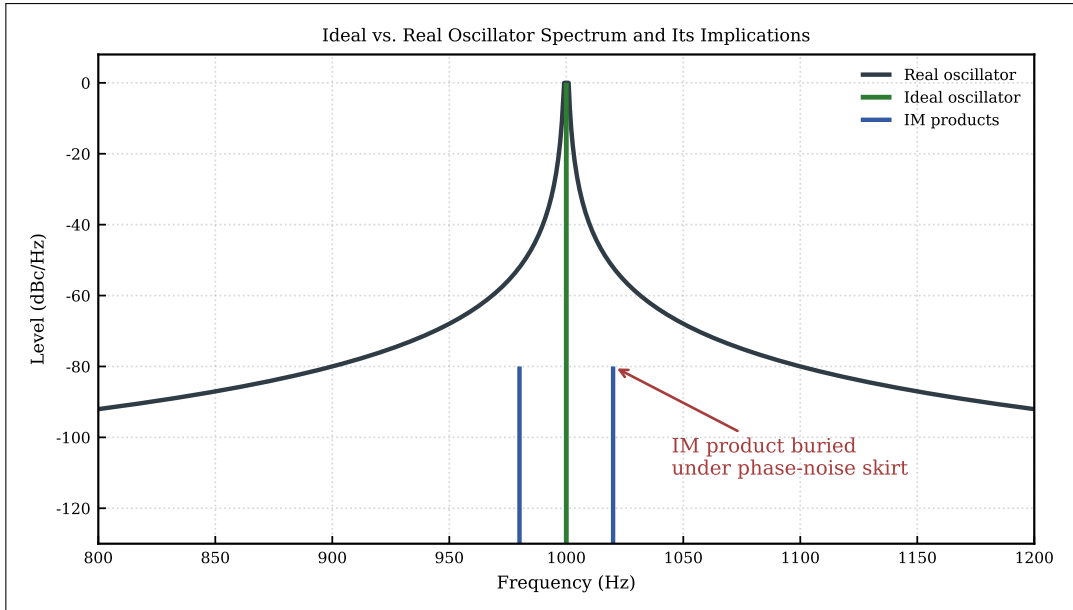


Figure 9: Phase noise in which IM products are obscured beneath the phase-noise skirt.

3.2 Naïve Solutions

A naïve fix is to notch the artefact at the carrier. As Figure 10 shows, a narrow notch suppresses the line but leaves the close-in phase-noise skirt essentially unchanged. Another approach is to widen the notch yet as Figure 11 shows, this suppresses both the carrier and the IM products. It appears that in order to develop a solution to the challenge, it is necessary to understand the mechanisms that generate the skirt prior to developing an effective cancellation strategy.

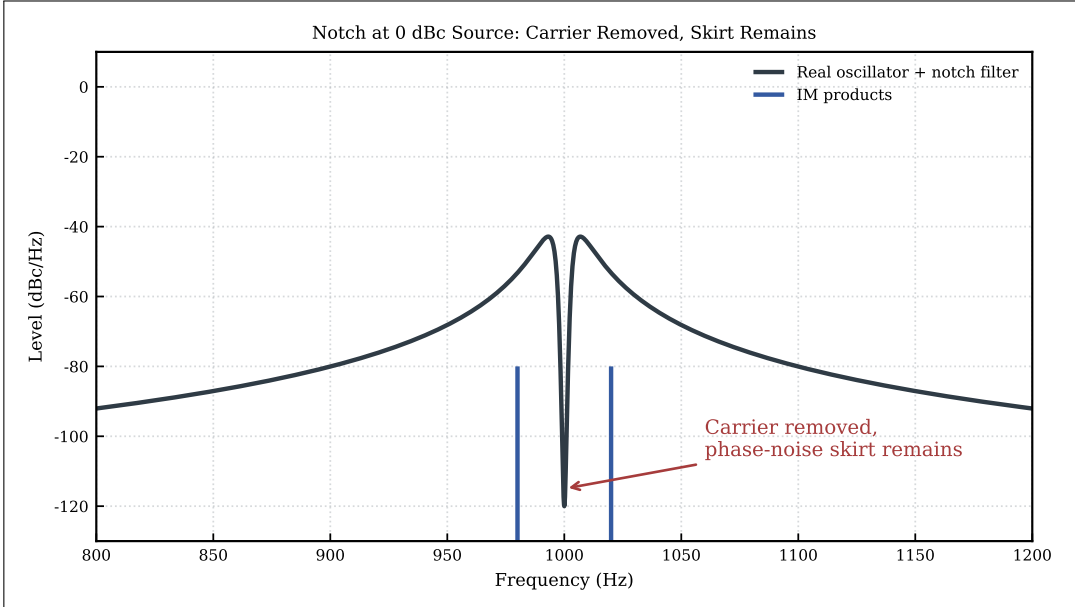


Figure 10: Narrow carrier notch removes the line but leaves the phase noise skirt intact.

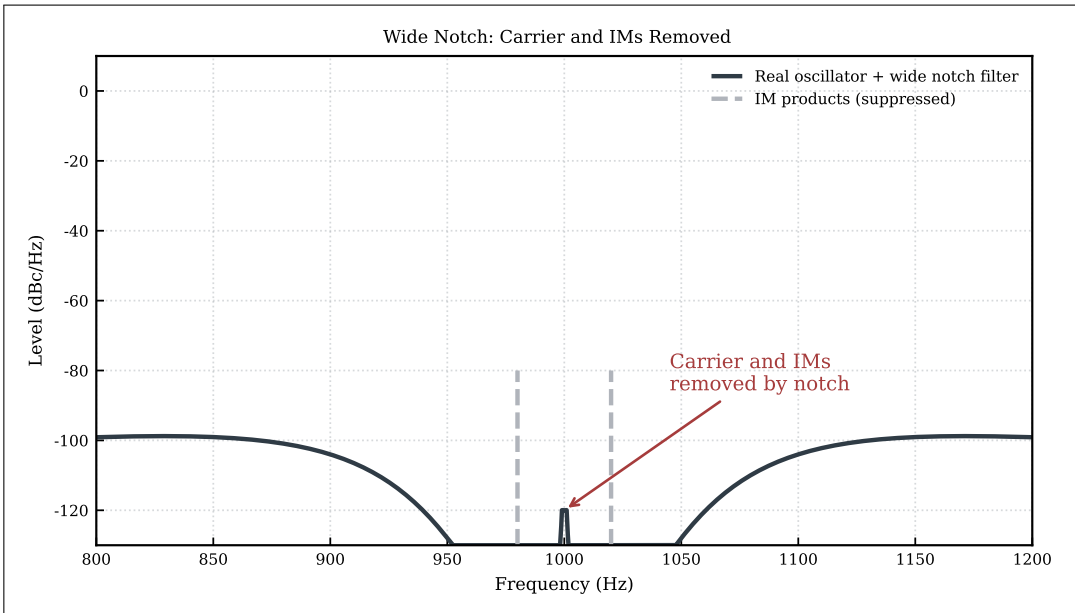


Figure 11: Wide notch filter suppresses both the carrier and nearby IM products.

3.3 Modelling the Artefact

Before modelling the artefact's phase-noise skirt, it is helpful to recall a basic property of oscillators. Real oscillators are linear time-varying (LTV) systems; an impulsive perturbation injected into the oscillatory system produces a lasting shift in the oscillation's phase [16]. Figure 12 displays this effect. Depending on when the impulse is injected within the cycle (often referred to as the limit-cycle), the phase shift is an advance or a lag [16]². This cycle-dependent sensitivity is formalised by the impulse sensitivity function (ISF) of the oscillator [16].

²The foregoing has one exception: an impulse applied at the amplitude peaks yields zero phase shift.

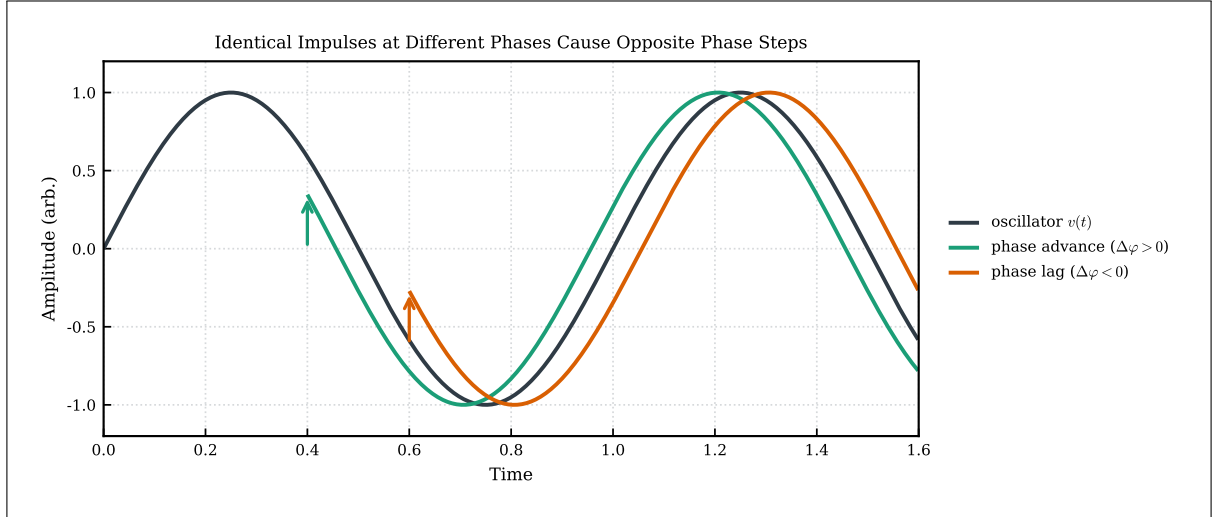


Figure 12: Impulse injection causes phase modulation whose sign and magnitude depend on timing of injection.

Figure 13 presents a more rigorous explanation. The phase response to an injected source $i(t)$ can be written with an LTV phase kernel [16]

$$h_\phi(t, \tau) = \frac{\Gamma(\omega_0 \tau)}{q_{\max}} u(t - \tau), \quad (5)$$

where:

- t is the observation time,
- τ is the integration variable (perturbation time),
- $\Gamma(\cdot)$ is the ISF, dimensionless and periodic over one cycle,
- ω_0 is the nominal angular frequency,
- q_{\max} is a normalising charge displacement along the limit cycle,
- $u(\cdot)$ is the unit step enforcing causality.

The resulting phase deviation accumulates the ISF-weighted perturbations:

$$\phi(t) = \int_{-\infty}^{\infty} h_\phi(t, \tau) i(\tau) d\tau = \frac{1}{q_{\max}} \int_{-\infty}^t \Gamma(\omega_0 \tau) i(\tau) d\tau, \quad (6)$$

where $i(t)$ is the injected perturbation entering the oscillatory system.

For a single impulse $i(t) = I_0 \delta(t - t_0)$, the phase step is

$$\Delta\phi = \frac{I_0}{q_{\max}} \Gamma(\omega_0 t_0), \quad (7)$$

where:

- I_0 is the impulse area,
- t_0 the injection time.

This recovers the advance-lag behaviour demonstrated in Figure 12.

The observable output is a sinusoidal carrier with time-varying phase,

$$v(t) = \cos(\omega_0 t + \phi(t)), \quad (8)$$

which, for $|\phi(t)| \ll 1$, reduces to:

$$v(t) \approx \cos(\omega_0 t) - \phi(t) \sin(\omega_0 t). \quad (9)$$

This makes the spectral link explicit: fluctuations in $\phi(t)$ appear as modulation sidebands around the carrier.

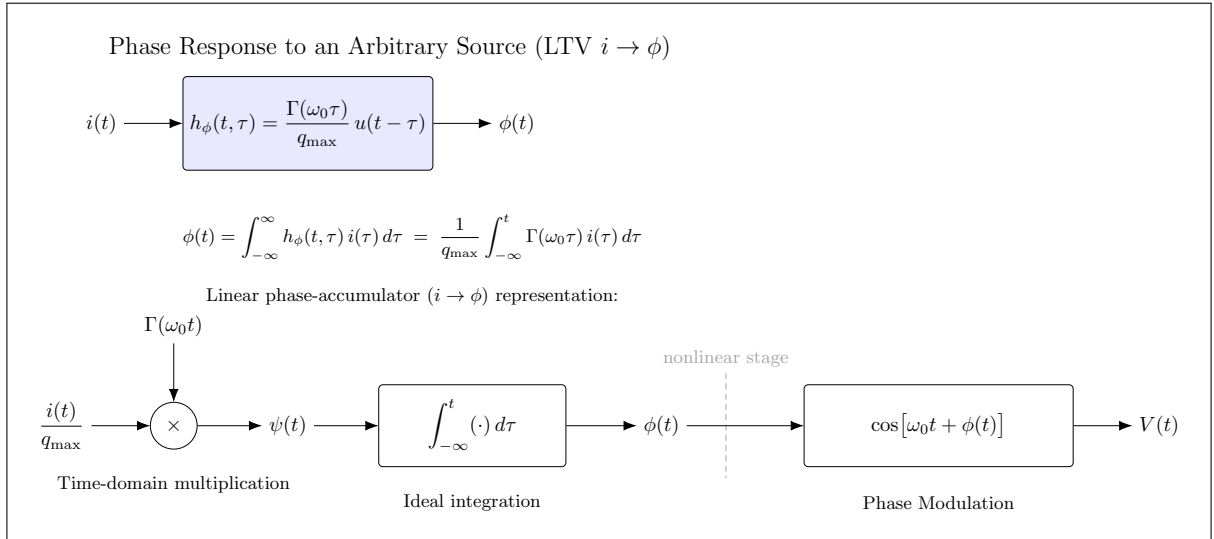


Figure 13: Time-domain view of phase sensitivity and modulation (adapted from [15]).

Having established the link between $\phi(t)$ and sidebands, the next question is which parts of the source noise shape the skirt. Figure 14 addresses this by expanding the oscillator's cycle-dependent sensitivity over one period [15]:

$$\Gamma(\omega_0 t) = c_0 + \sum_{n \geq 1} c_n \cos(n\omega_0 t), \quad (10)$$

where:

- c_0 is the DC (cycle-averaged) sensitivity,
- c_n are the harmonic sensitivity coefficients.

The source sampled by Γ can be taken as a typical combination of $1/f$ noise (dominant at low frequencies) and thermal noise (approximately white). The DC term c_0 therefore emphasises slow fluctuations and sets the steep, close-in part of the phase-noise skirt. The harmonic terms c_n pick up noise in small windows around $n\omega_0$ and fold it toward baseband, filling the outer regions of the skirt. Under small phase modulation, this baseband phase noise appears as symmetric skirts around the carrier in the output spectrum.

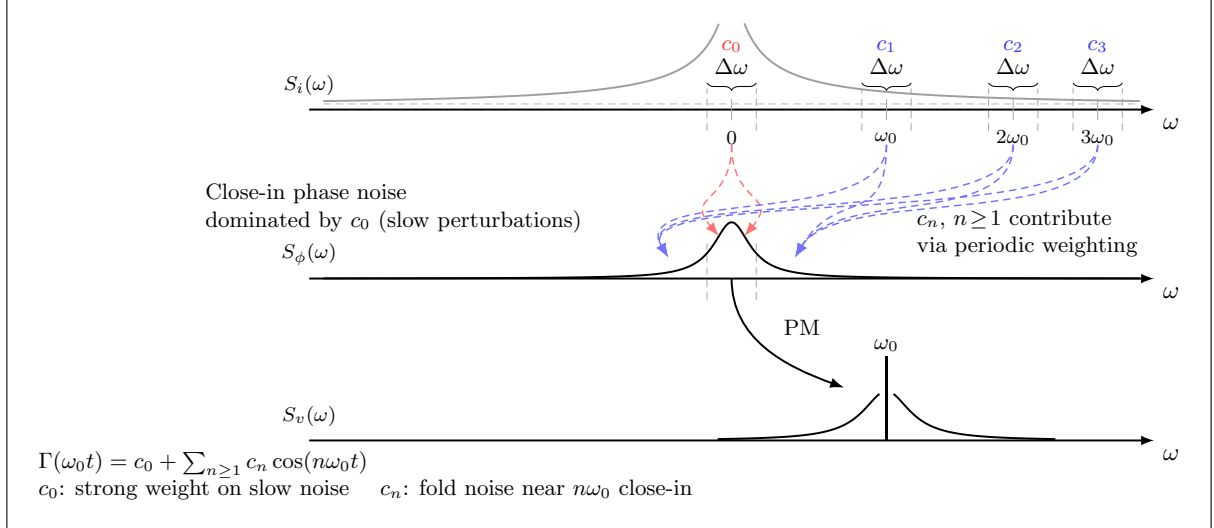


Figure 14: Frequency-domain view of phase-noise skirt formation (adapted from [15]).

The ISF picture above captures phase sensitivity of an autonomous oscillator. In the current setup, however, the stimulation drive is digitally synthesised and then passes through an electrode–tissue interface³. Two factors therefore shape the observed artefact skirt: (i) phase noise (due to jitter) from the clock that is generating the numerically controlled oscillator (NCO) [17], and (ii) slow variation of the electrode–tissue path, which behaves as a time-varying complex impedance and imposes both amplitude and phase modulation (AM/PM) on the tone [18]. This composition is shown in Figure 15.

In the sketch, the source block is written as

$$s(t) = A_0 \cos(\omega_0 t + \phi_{\text{NCO}}(t)), \quad (11)$$

where:

- A_0 is the nominal drive amplitude,
- ω_0 is the stimulation angular frequency,
- $\phi_{\text{NCO}}(t)$ represents source phase wander due to the clock generating the NCO.

The path block is represented as a slow, complex gain

$$G(t) = |G(t)| e^{j\psi(t)}, \quad (12)$$

³More precisely, the digital-to-analogue converter (DAC) output voltage is converted into a differential current by a current stimulator before reaching the electrodes.

where:

- $|G(t)|$ is a slowly varying amplitude,
- $\psi(t)$ is a slowly varying phase.

Combining the two yields the recorded artefact at the EEG amplifier input:

$$y(t) = |G(t)| A_0 \cos(\omega_0 t + \psi(t) + \phi_{\text{NCO}}(t)). \quad (13)$$

The practical consequence is clear: effective cancellation must track the artefact's amplitude and phase coherently. Once the stimulation signal is coherently tracked, the artefact's carrier and close-in skirt can be cancelled while leaving nearby IM products visible, as shown in Figure 16.

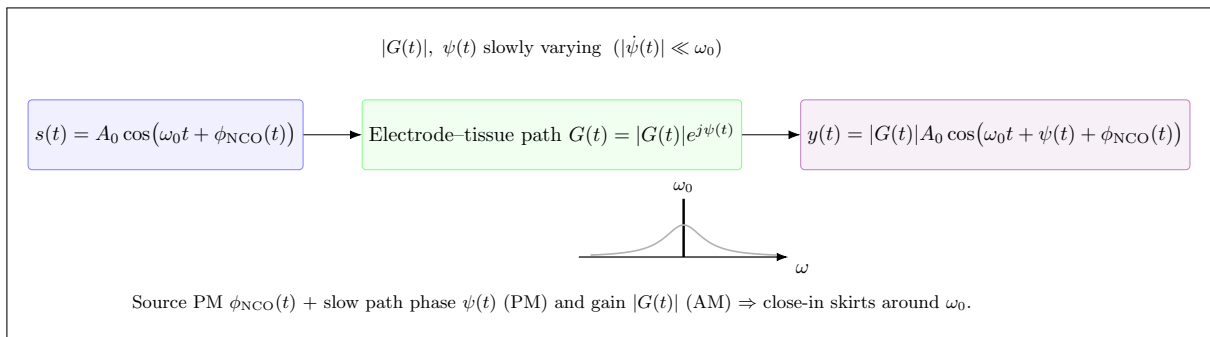


Figure 15: Sketch of the artefact signal model: clocked tone through a time-varying electrode–tissue impedance.

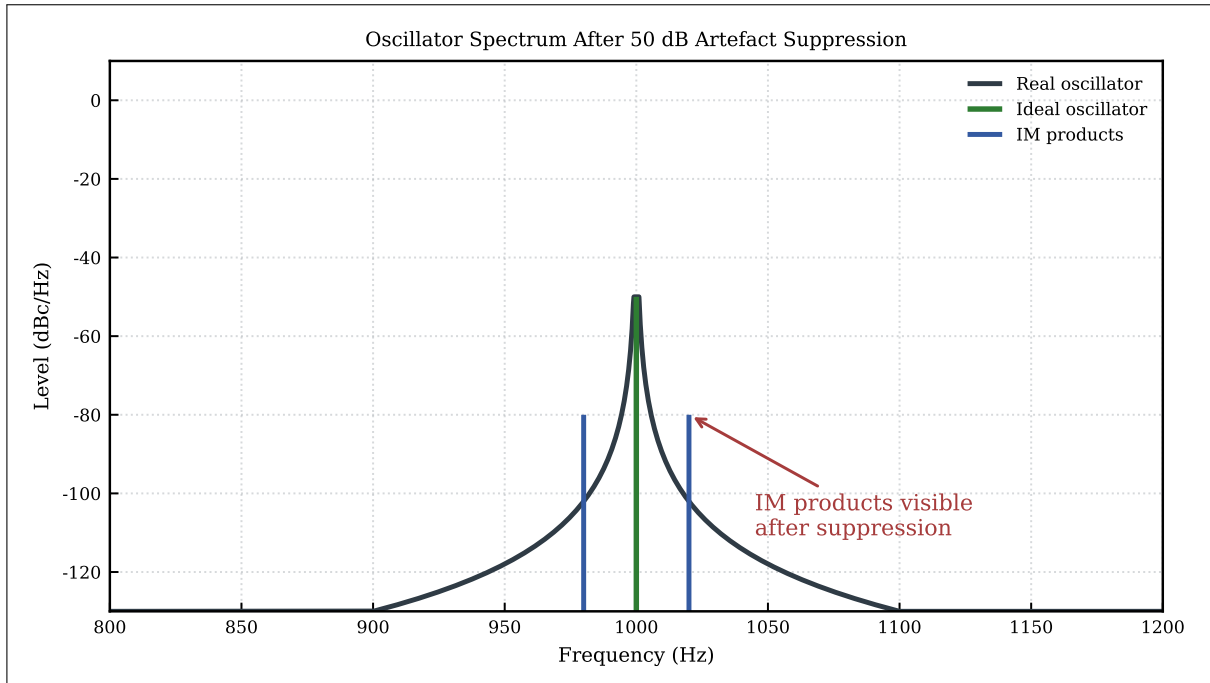


Figure 16: Coherent cancellation suppresses the carrier and close-in skirt, revealing adjacent IM sidebands.

Summary

- **Why it's hard:** the stimulation artefact masks cortical signals and carries a close-in, time-correlated phase-noise skirt that simple averaging cannot remove.
- **Naïve fixes fail:** a narrow notch drops only the carrier line (skirt remains); a wide notch kills the skirt and the nearby putative sidebands.
- **Where the skirt comes from:** clock jitter and a slowly changing electrode–tissue path impose amplitude/phase wander on the tone, spreading energy around the carrier.
- **Practical framing:** this is not a “remove a single frequency”; it’s a “track and cancel a time-varying complex tone” (amplitude & phase).
- **Consequence:** a workable approach must estimate that drift and subtract a synchronised anti-signal while preserving neighbouring spectral content.
- **Bridge:** motivates a carrier-referenced cancellation loop that tracks amplitude and phase over time (specific realisation introduced next).

4 Method

This section introduces three complementary views of the coherent cancellation mechanism: a control system model, a signal processing model, and a physical model. Each provides insight into the mechanism and informs considerations for its optimal implementation.

4.1 Control System Model

In order to provide an intuitive explanation of the cancellation mechanism, it is useful to begin with a familiar control structure: the phase-locked loop (PLL). As shown in Figure 17a, a PLL comprises a phase detector, a loop filter, and a voltage-controlled oscillator (VCO) in feedback [13]. With a reference clock at the detector, the loop drives the VCO so that its output phase locks to the reference and the single error signal measures phase difference. This is useful but limited for artefact cancellation because it does not estimate amplitude.

An analogous vector-locked loop (VLL), shown in Figure 17b, is proposed to address this limitation. It replaces the single phase detector with an I/Q demodulator referenced to the same clock. The demodulator yields two baseband signals, I (in-phase) and Q (quadrature). After suitable loop filtering, I and Q provide a complex estimate of the artefact envelope. Remodulating this estimate synthesises a tone that tracks the amplitude and phase of the reference, enabling coherent subtraction of both the carrier and the close-in skirt⁴.

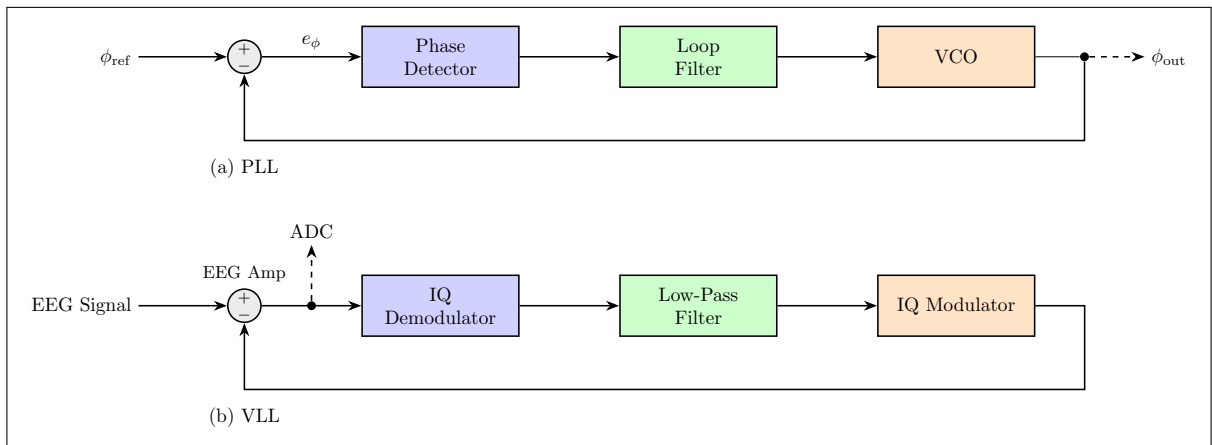


Figure 17: Block diagram comparison between a conventional PLL (a) and an analogous VLL (b) for artefact cancellation in EEG. Colour coding highlights the functional correspondence between the two loop architectures.

4.2 Signal Processing Model

To avoid ambiguity left by the analogy, Figure 18 presents the cancellation architecture as a lock-in loop surrounding the EEG amplifier. The amplifier’s output (i.e., the instantaneous residual) first passes through a band-pass filter centred on the stimulation frequency. This filter is not for “clean-up”; it confines the detector to the carrier band so that off-band components are not misinterpreted as on-carrier energy. The band-limited residual is then demodulated against a local oscillator (LO) phase-locked to the stimulation: one mixer with $\cos \omega_0 t$ (in-phase)

⁴A PLL’s output is typically taken from the VCO, whereas in the present setup the cancellation path is tapped at the node between the EEG amplifier and the I/Q demodulator.

and one with $\sin \omega_0 t$ (quadrature). Each mixer output is low-pass filtered to yield slowly varying I and Q , which together estimate the complex envelope of the artefact at the carrier. After low-pass filtering to remove high-frequency mixing products, the same LO is used to remodulate these estimates, forming $I \cos \omega_0 t + Q \sin \omega_0 t$. This synthesised tone is injected at the EEG amplifier input as the cancellation signal. Because the LO is coherent with the stimulation and the loop adjusts I and Q continuously, the injected signal tracks the near-instantaneous amplitude and phase of the artefact carrier⁵. In a closed loop, the estimate should, in principle, converge to an accurate extraction of the artefact.

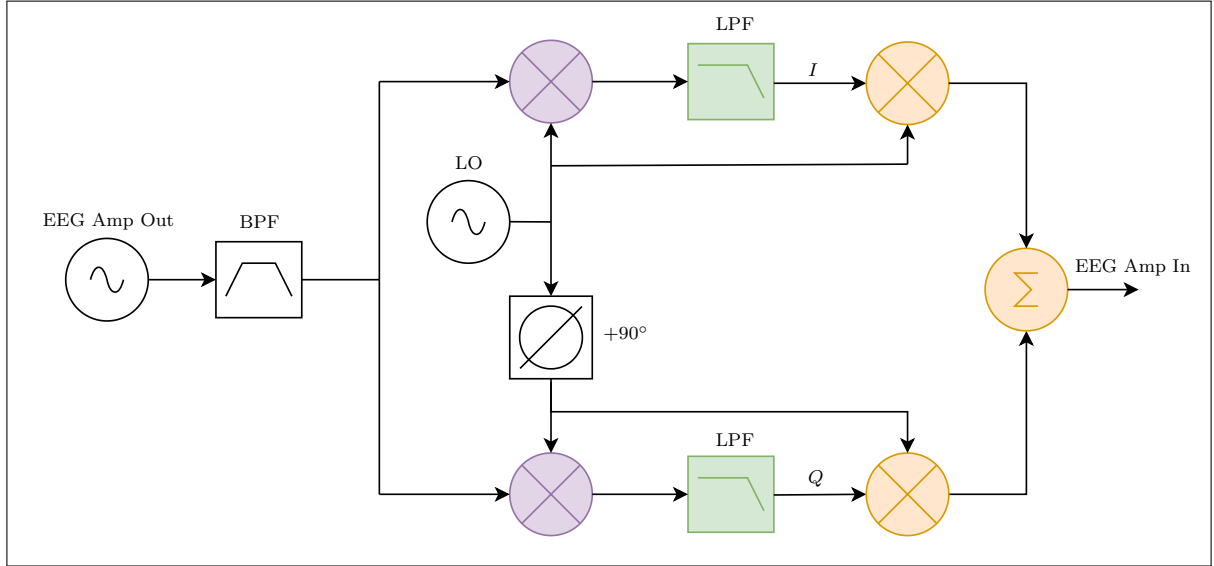


Figure 18: Lock-in amplification with IQ demodulation and remodulation.

4.3 Physical Model

To complement the control and signal processing views, a physical model of the cancellation mechanism is introduced to provide further insight. For analytical tractability, the artefact $y(t)$ is here simplified from the more detailed electrode-path model of Figure 15 to

$$y(t) = A(t) \cos(\omega_0 t + \theta(t)), \quad (14)$$

where $A(t)$ and $\theta(t)$ vary slowly relative to ω_0 .

The canceller synthesises

$$\hat{y}(t) = \alpha_I(t) \cos(\omega_0 t) + \alpha_Q(t) \sin(\omega_0 t), \quad (15)$$

with $\alpha_I(t)$ and $\alpha_Q(t)$ serving as the internal complex envelope estimates. The residual is defined as

$$r(t) = y(t) - \hat{y}(t),$$

⁵In practice, instantaneous tracking is not possible even in a continuous model, since the loop's response is limited by the time constant of the low-pass filter.

and forms the lock-in detector error channels by orthogonal projection and low-pass filtering

$$e_I(t) = \text{LPF}\{ r(t) \cos(\omega_0 t) \}, \quad (16)$$

$$e_Q(t) = \text{LPF}\{ r(t) \sin(\omega_0 t) \}. \quad (17)$$

Assuming slow variations, one obtains the approximate relations

$$e_I(t) \approx \frac{A}{2} \cos \theta - \alpha_I(t), \quad (18)$$

$$e_Q(t) \approx \frac{A}{2} \sin \theta - \alpha_Q(t). \quad (19)$$

A simple proportional adaptation closes the loop through first-order differential equations

$$\frac{d\alpha_I}{dt} = \gamma e_I(t), \quad (20)$$

$$\frac{d\alpha_Q}{dt} = \gamma e_Q(t), \quad (21)$$

with loop gain $\gamma > 0$. The first-order dynamics exhibit exponential decay to equilibrium:

$$\alpha_I(t) = \frac{A}{2} \cos \theta + (\alpha_I(0) - \frac{A}{2} \cos \theta) e^{-\gamma t}, \quad (22)$$

$$\alpha_Q(t) = \frac{A}{2} \sin \theta + (\alpha_Q(0) - \frac{A}{2} \sin \theta) e^{-\gamma t}, \quad (23)$$

so that

$$\boxed{\alpha_I(t) + j \alpha_Q(t) \rightarrow \frac{A}{2} e^{j\theta}}. \quad (24)$$

In the noiseless case the detector errors satisfy $e_I(t) \rightarrow 0$ and $e_Q(t) \rightarrow 0$, while the internal states α_I, α_Q converge to DC values equal to the artefact's complex envelope. The synthesised $\hat{y}(t)$ then coherently matches $y(t)$. This idealised result demonstrates exponential convergence to the correct envelope but also reveals a limitation: if the residual were perfectly nulled, the detector would lose its coherent reference and the loop could no longer adapt. The implications of this limitation will become apparent in the next section.

Summary

- **Goal:** coherently estimate and cancel the artefact's amplitude and phase at the carrier, not just the tone.
- **Control view (VLL):** generalises a PLL by locking the complex envelope of the artefact rather than just phase, enabling coherent cancellation of the carrier and its close-in phase-noise skirt.
- **Signal-processing view:** band-pass around the carrier \rightarrow I/Q demodulation with a coherent LO \rightarrow low-pass to get slow envelope estimates \rightarrow re-modulate and subtract; nearby spectral content is preserved.
- **Physical intuition:** internal I and Q states adapt until the synthesised tone matches the artefact's amplitude and phase; cancellation deepens as alignment improves.
- **Bridge:** the physical model flags a potential observability caveat at very deep nulls; subsequent sections examine its practical relevance in analogue versus digital realisations.

5 Analogue Simulation

Having established the conceptual nulling mechanism, it is instructive to test its performance through analogue simulation. This section presents the system's building blocks, the complete schematic, evaluated topologies that were later discarded, and the resulting simulation outcomes.

5.1 Circuit Building Blocks

Figure 19 shows the building blocks that collectively model the experimental setup. These are: **A** (buffer), **B** (inverting amplifier), **C** (third-order RC low-pass filter), **D** (summing amplifier), **E** (second-order active band-pass filter), **F** (difference amplifier), **G** (non-inverting amplifier), **H** (mixer), and **I** (phase shifter). Together with decoupling capacitors, these modules form the complete schematic shown in Figure 20. All elements are idealised except the mixer (**H**), which is instantiated with the AD633 SPICE macromodel to provide a realistic multiplier characteristic.

5.2 Schematic

The schematic in Figure 20 realises the cancellation mechanism at circuit level. It is presented in three parts: the closed-loop path, an empirical demonstration of its limitations, and the complementary open-loop path.

5.2.1 Closed-Loop Path

The green-highlighted path in Figure 20 corresponds to the closed-loop architecture introduced in the Method section. The sequence is as follows:

1. The residual from the EEG amplifier enters block **E**, a second-order active band-pass filter centred on the stimulation frequency. This confines detection to the carrier, excluding off-band components.
2. The filtered tone is split into two parallel mixers (**H**), driven by an LO coherent with the stimulation: one with cosine (in-phase) and one with sine (quadrature).
3. Each mixer output passes through a gain stage (**G**) and then a third-order RC low-pass filter (**C**), which rejects high-frequency terms and yields slowly varying I and Q . These form the loop's internal estimates of the artefact envelope.
4. To generate the cancellation signal, I and Q are remodulated against the same LO using another pair of mixers (**H**). Their outputs are summed in **D**, producing a sinusoid whose instantaneous amplitude and phase are set by I and Q .
5. The summed tone passes through a decoupling capacitor and a buffer (**A**). The buffer isolates the closed-loop (green) from the open-loop (orange) part of the circuitry, which will be described shortly.
6. The buffered cancellation enters one input of a difference amplifier (**F**). At the other input of **F**, the EEG signal is applied after inversion by **B**. This inversion ensures that the artefact is presented in opposite polarity,

so that **F** performs subtraction (rather than addition) between the amplified artefact and the synthesised cancellation tone.

7. The decoupling capacitor between **D** and **A** prevents DC offsets from biasing the nulling stage.

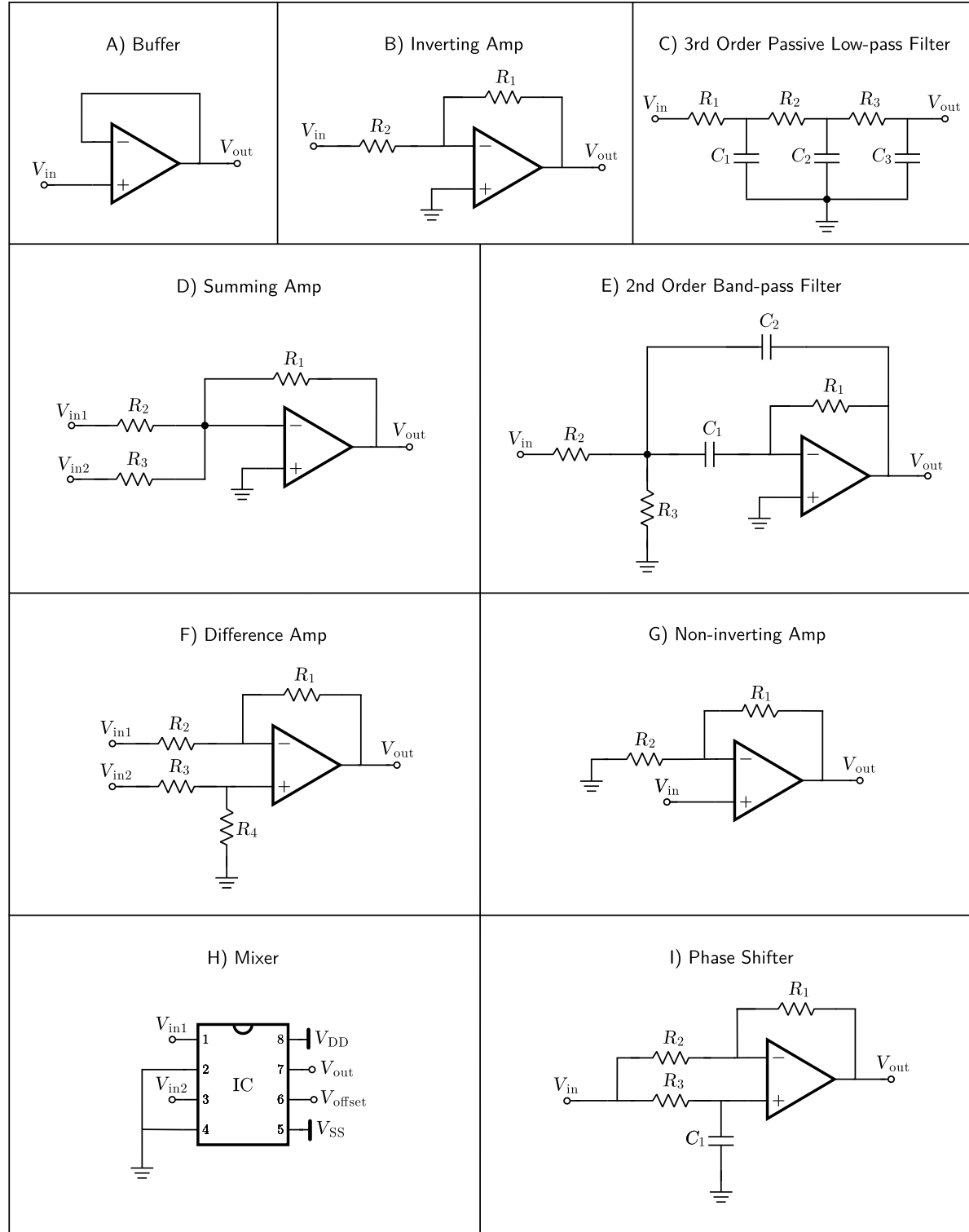


Figure 19: Circuit primitives composing the system-level LTspice model.

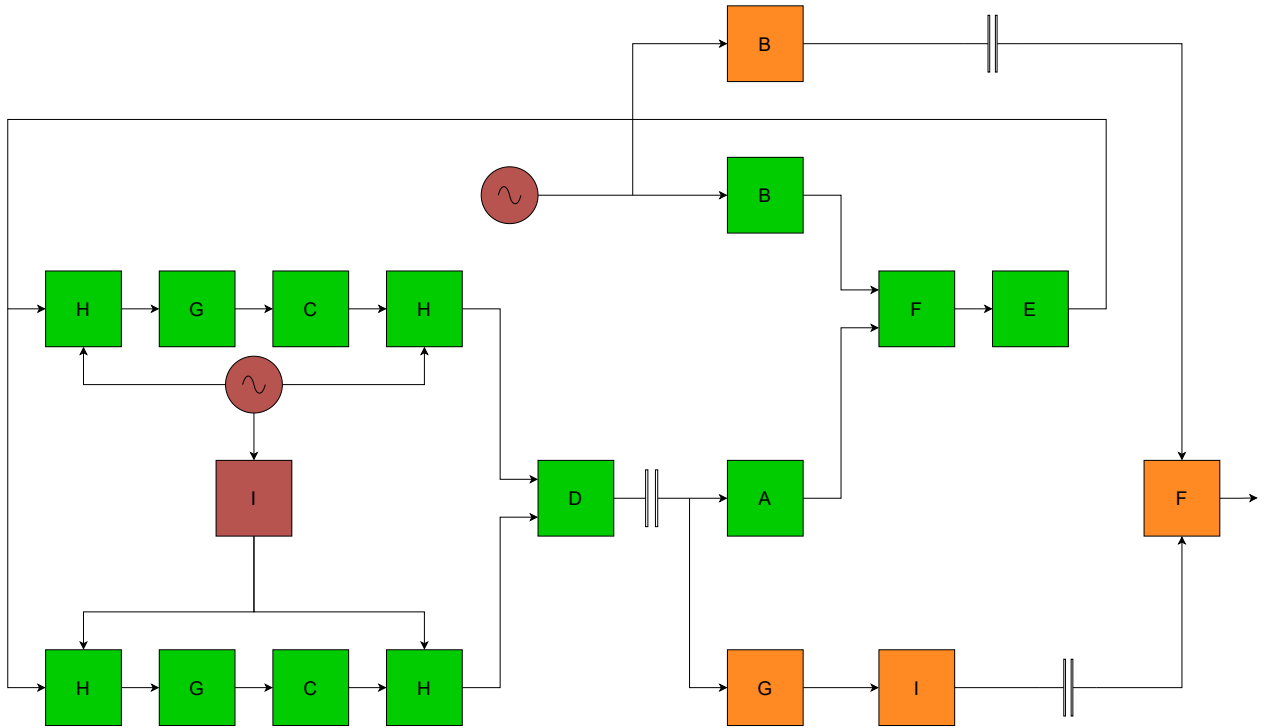


Figure 20: System-level LTspice model built from circuit primitives from Figure 19.

5.2.2 Limits of Closed-Loop Path

The behaviour of the cancellation loop depends critically on the choice of loop gain. If the gain is too small, the I and Q states converge slowly but reliably (see Figure 21), producing a cancellation tone that is much weaker than the artefact (see Figure 24). In this overdamped regime the system is stable, but a large residual remains at the detector input.

At the opposite extreme, if the gain is set too high, the loop attempts to drive the cancellation tone up to the artefact's amplitude but overshoots, causing instability (see Figure 26). The I and Q states diverge under the influence of noise and offsets, and the loop enters runaway behaviour (see Figure 23).

Between these extremes lies a regime of stable underdamped response. Here, the I and Q states converge rapidly to their equilibrium values (see Figure 22), and the cancellation tone tracks the artefact with reasonable accuracy (Figure 25). However, even in this case the cancellation signal falls short of the artefact's amplitude, so a residual remains.

These limitations reflect the observability constraint discussed in the Physical Model subsection of the Method section: the lock-in detector requires a coherent residual to correlate against the LO. As the residual decreases, noise and offsets dominate the correlation, corrupting the I and Q estimates; with high loop gain, these spurious values destabilise the system. The practical consequence is that the feedback loop alone cannot null the artefact completely. Regardless of fine loop gain tuning, the cancellation signal remains weaker than the artefact, leaving a residual. To achieve deeper suppression while maintaining stability, an auxiliary feedforward path is required.

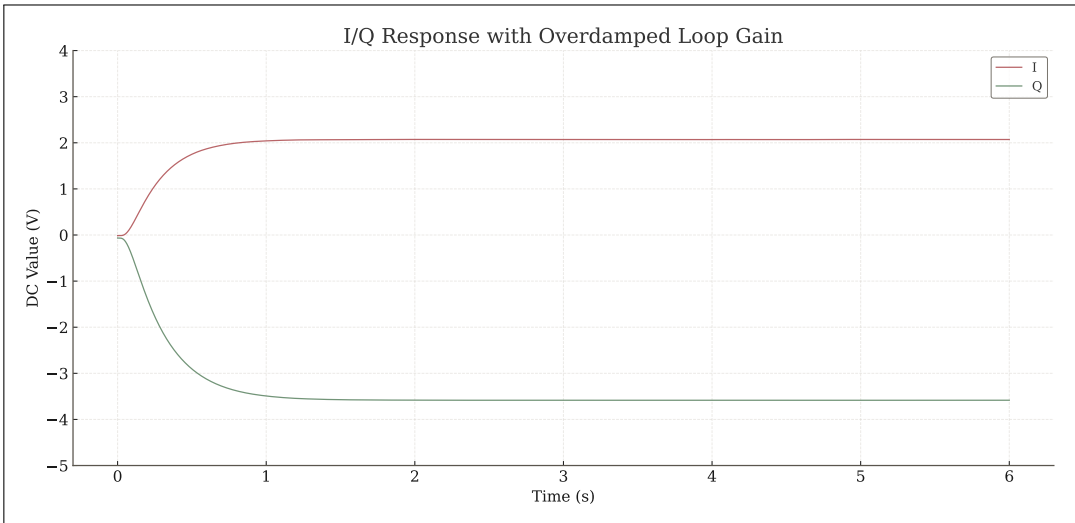


Figure 21: I and Q trajectories in the overdamped regime: slow but stable convergence.

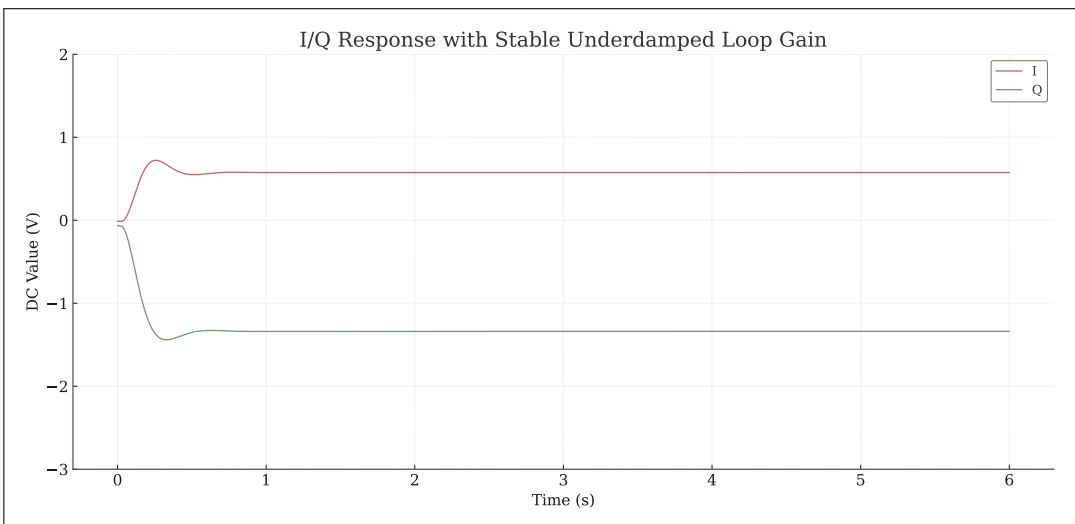


Figure 22: I and Q trajectories in the stable underdamped regime: rapid convergence to equilibrium values.

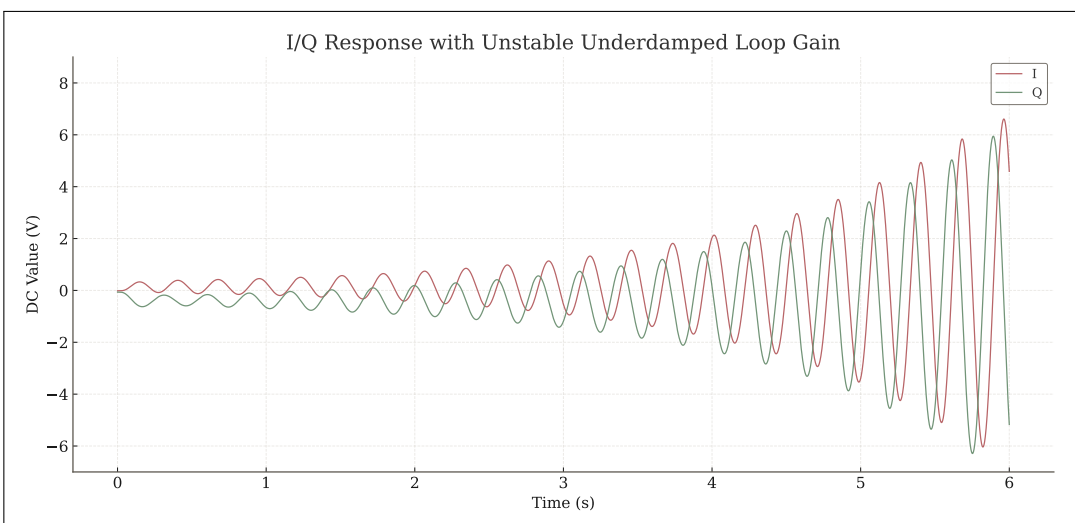


Figure 23: I and Q trajectories in the unstable underdamped regime: divergence under noise and offsets.

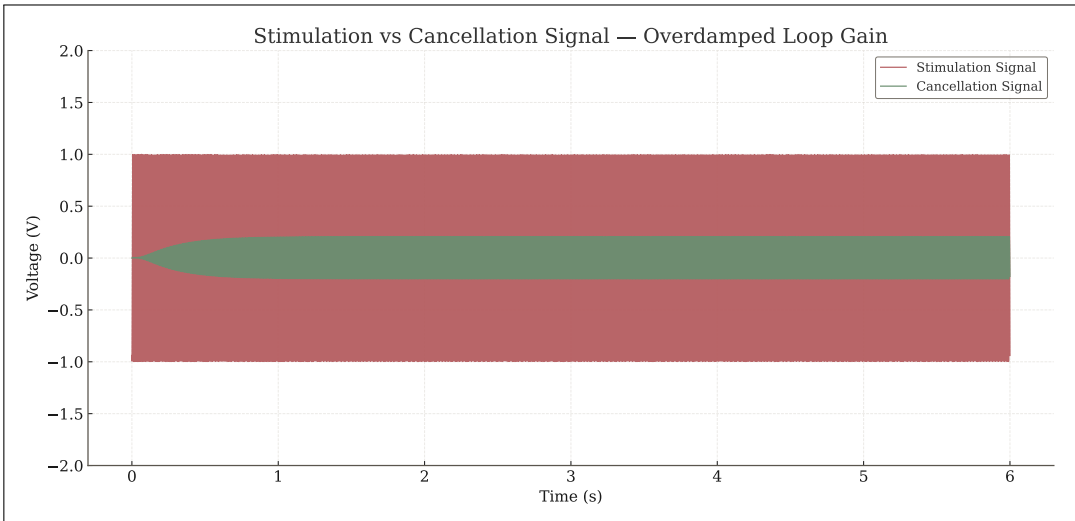


Figure 24: Residual spectrum in the overdamped regime: weak cancellation tone leaves strong artefact.

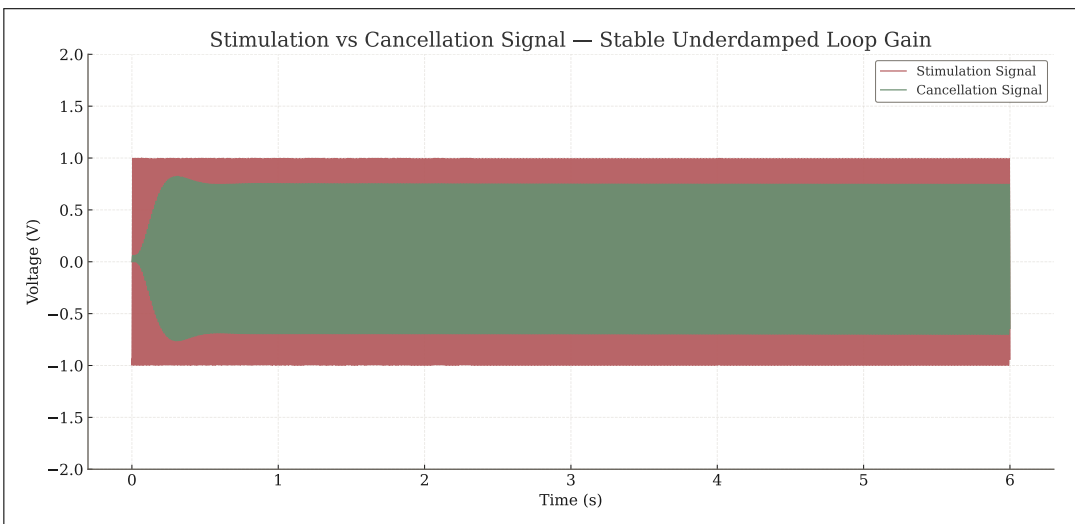


Figure 25: Residual spectrum in the stable underdamped regime: effective tracking but incomplete suppression.

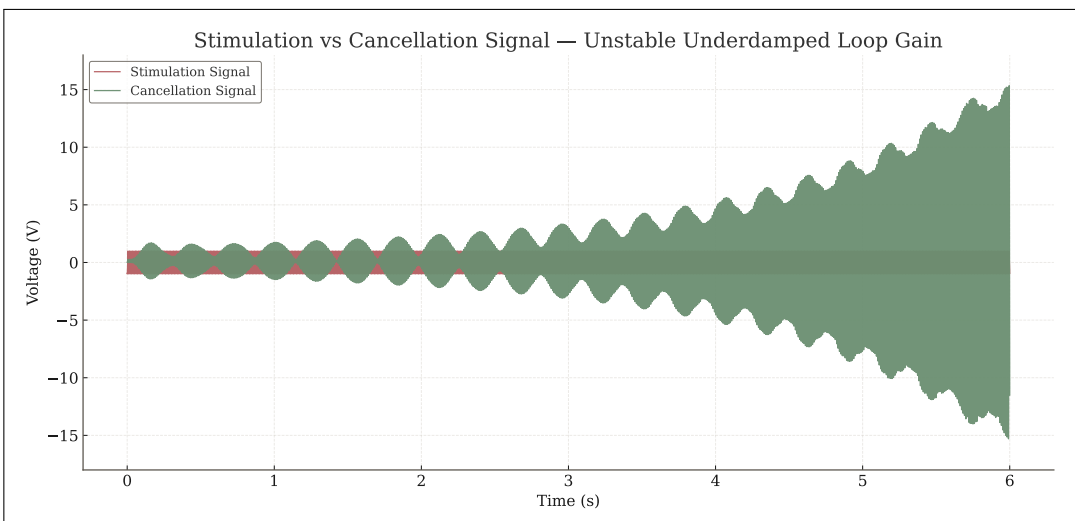


Figure 26: Residual spectrum in the unstable underdamped regime: loop runaway prevents cancellation.

5.2.3 Open-Loop Path

The orange path in Figure 20 addresses this limitation. Its purpose is to complement the closed-loop path by restoring the depth of cancellation that the feedback loop alone cannot achieve without losing observability. The arrangement works as follows:

1. The artefact signal is sent through an inverter (**B**) and a decoupling capacitor, then into a dedicated difference amplifier (**F**). This forms the reference channel against which the feedforward branch is compared.
2. In parallel, the synthesised cancellation tone is diverted before entering the feedback buffer (**A**).
3. Instead of being injected directly, the diverted signal is first scaled in amplitude by a controlled non-inverting stage (**G**).
4. The amplitude-scaled signal is then phase-adjusted by a phase shifter (**I**).
5. After passing through a decoupling capacitor, the conditioned signal enters the second difference amplifier (**F**), where it is subtracted from the artefact reference.

In summary, the closed loop ensures stable tracking by leaving a small residual pilot, while the open loop restores suppression depth by re-scaling and phase-adjusting the converged cancellation tone.

5.3 Redundant Complexity

During early simulation, a consistent dependence of the cancellation signal amplitude on the artefact phase was observed. This behaviour initially suggested a limitation of the I/Q feedback technique, potentially due to nonlinearities or phase-dependent gain mismatch in the loop. To compensate for this, a pair of automatic gain control (AGC) circuits were implemented. These were based on matched JFETs and precision rectifiers, and used a differential DC comparison between the artefact signal and the cancellation signal to drive a gain-adjustment mechanism. A secondary AGC stage was also introduced at the input of the subtractor unit to prevent amplitude drift from propagating into the lock-in amplifier path.

Subsequent investigation revealed, however, that the amplitude variation was caused by the absence of DC offsets in the AD633 SPICE models. Without these offsets, the simulated multipliers produced unintended cross-terms during mixing, leading to amplitude–phase coupling in the I/Q path. Once the models were corrected by introducing a fixed -2.6 mV DC offset at the voltage offset input of each mixer block (**H**), the system exhibited stable amplitude and phase locking across a wide artefact amplitude range (0.5 V to 5 V). The AGC circuits, albeit functional, were ultimately rendered unnecessary.

5.4 Performance

To test the behaviour of the analogue model, deliberate perturbations were applied to the stimulation signal in LTspice. Two cases were examined: step changes in phase and step changes in amplitude. In each case, the evolution of the residual error and the internal *I/Q* states was monitored.

Figure 27 shows the cancellation response when the stimulation phase is stepped. The residual exhibits a transient deviation at each phase jump, after which the loop restores cancellation. A closer view in Figure 28 highlights the underdamped settling of the error following the step. This is consistent with the loop dynamics derived earlier: the I/Q states adjust gradually to the new phase, leaving a brief overshoot before convergence. The corresponding I/Q trajectories are plotted in Figure 29. As expected, the states shift to new equilibrium values determined by the updated stimulation phase.

An analogous simulation was performed with step changes in stimulation amplitude. The residual behaviour is shown in Figure 30. Each amplitude increase produces a transient overshoot, after which the cancellation tone scales to the new level. The close-up in Figure 31 again reveals underdamped settling, similar to the phase-step case. Figure 32 shows the associated I/Q dynamics. Both states expand or contract in magnitude while preserving their relative phase, converging toward the new envelope value. This demonstrates that the loop tracks amplitude variations as reliably as phase variations.

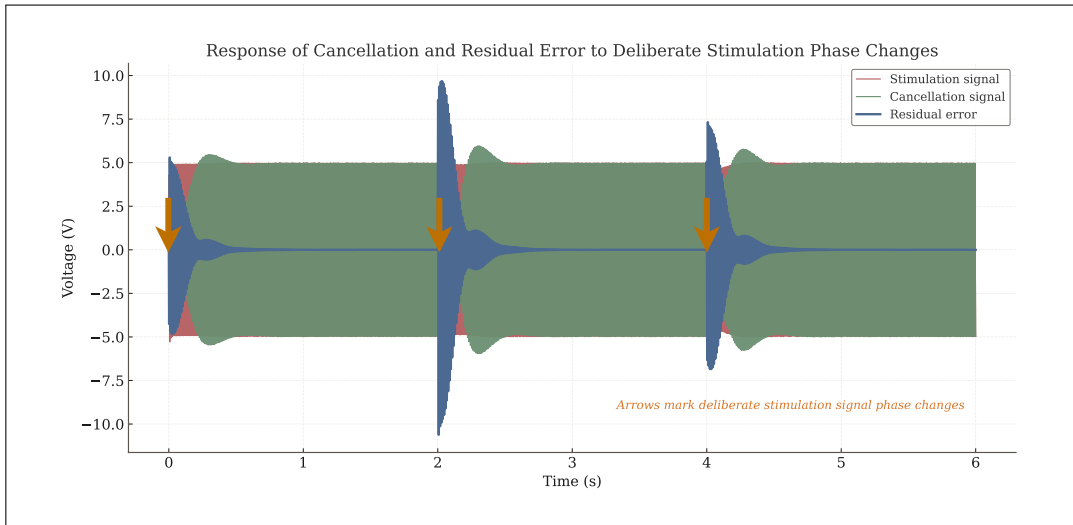


Figure 27: LTspice simulation of cancellation response to deliberate stimulation phase changes.

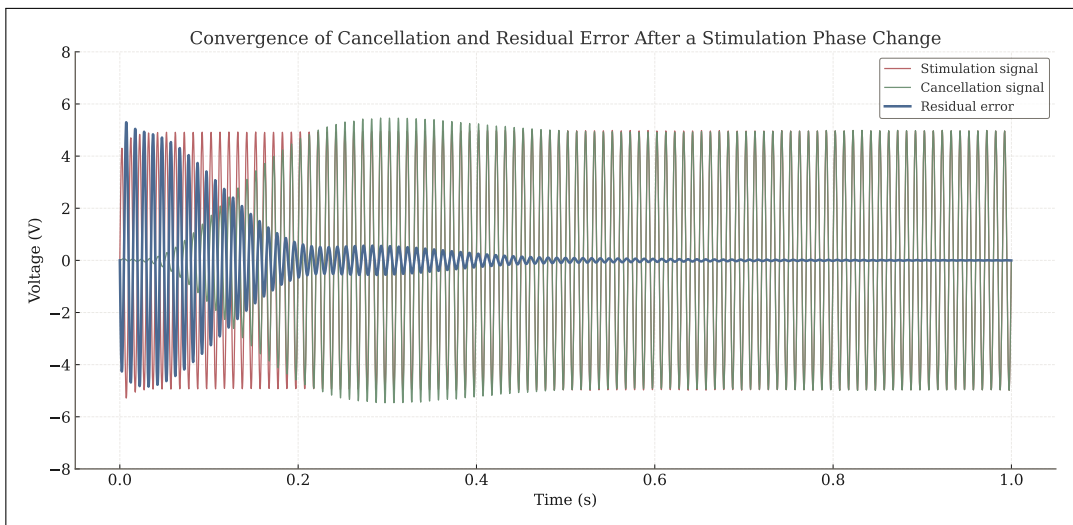


Figure 28: Close-up LTspice simulation of cancellation response to deliberate stimulation phase changes.

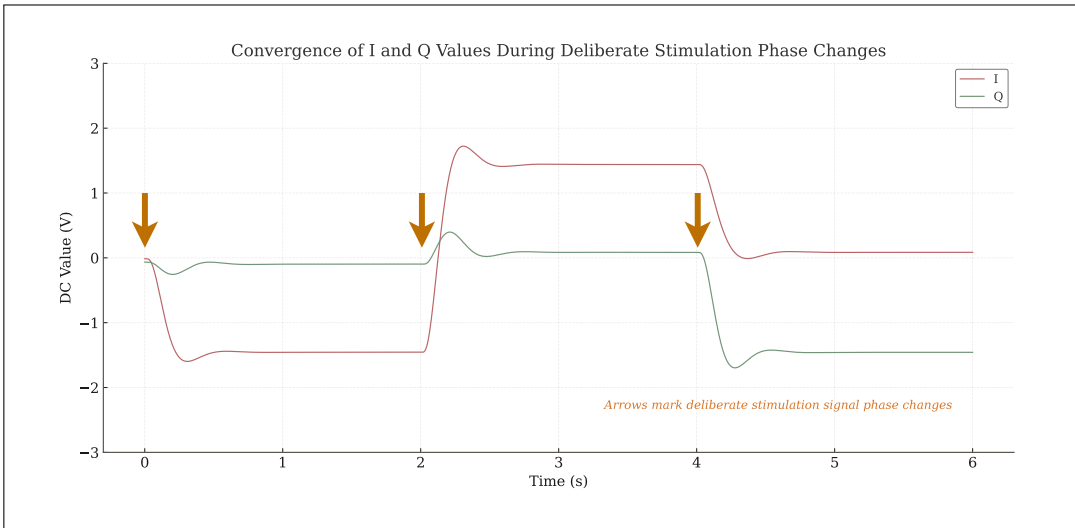


Figure 29: LTspice simulation of I/Q convergence during stimulation phase changes.

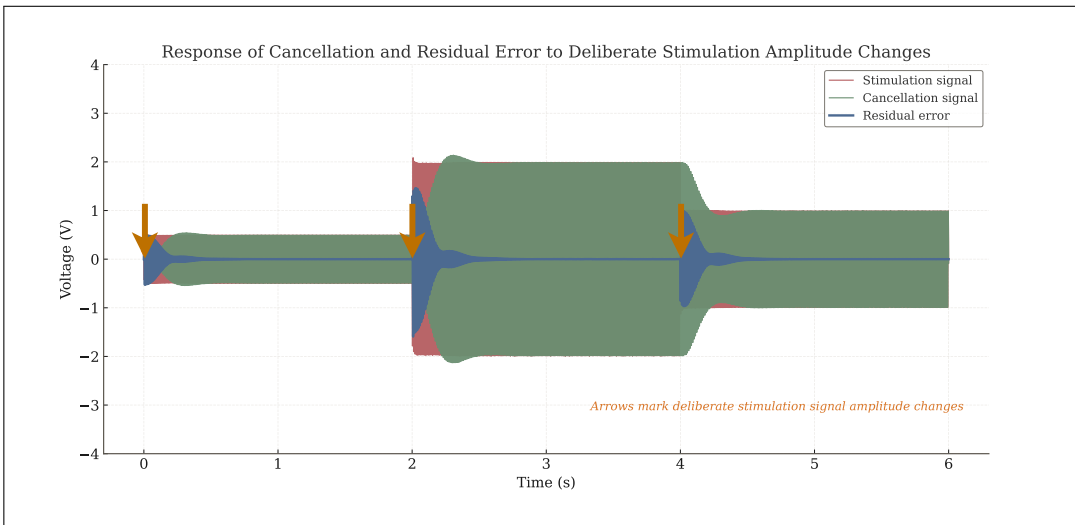


Figure 30: LTspice simulation of cancellation response to deliberate stimulation amplitude changes.

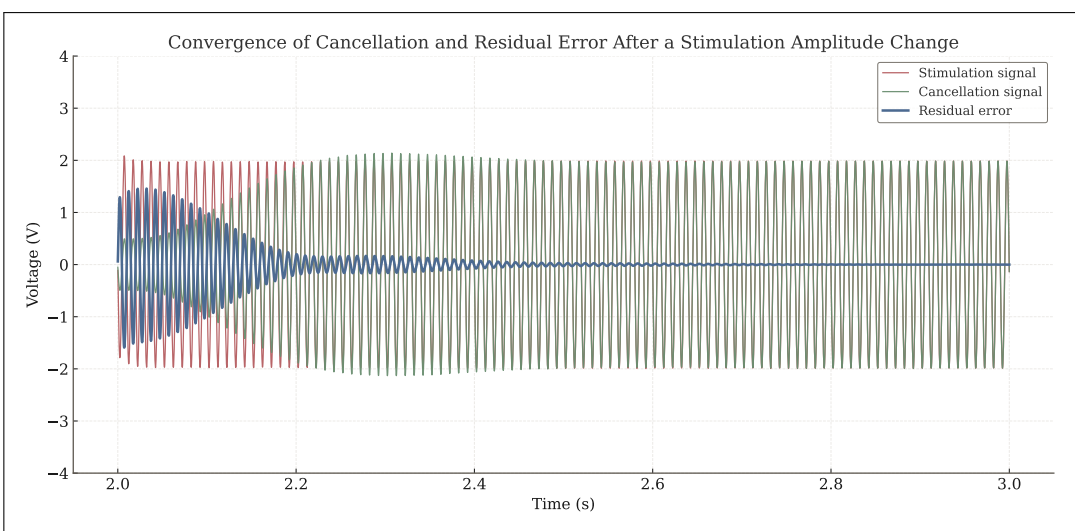


Figure 31: Close-up LTspice simulation of cancellation response to deliberate stimulation amplitude changes.

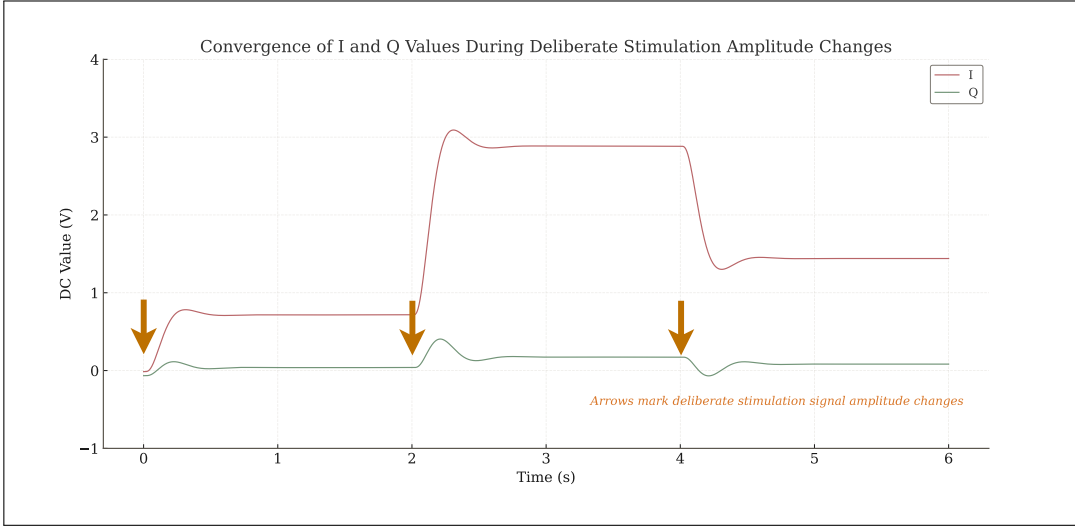


Figure 32: LTspice simulation of I/Q convergence during stimulation amplitude changes.

To quantify overall suppression, FFTs of the residual were taken before and after cancellation. As shown in Figure 33, the observed attenuation is below 60 dB⁶. This should be regarded as a best case, since all circuit elements in the simulation are idealised apart from the mixers. In practice, real hardware will introduce additional nonidealities that further degrade performance.

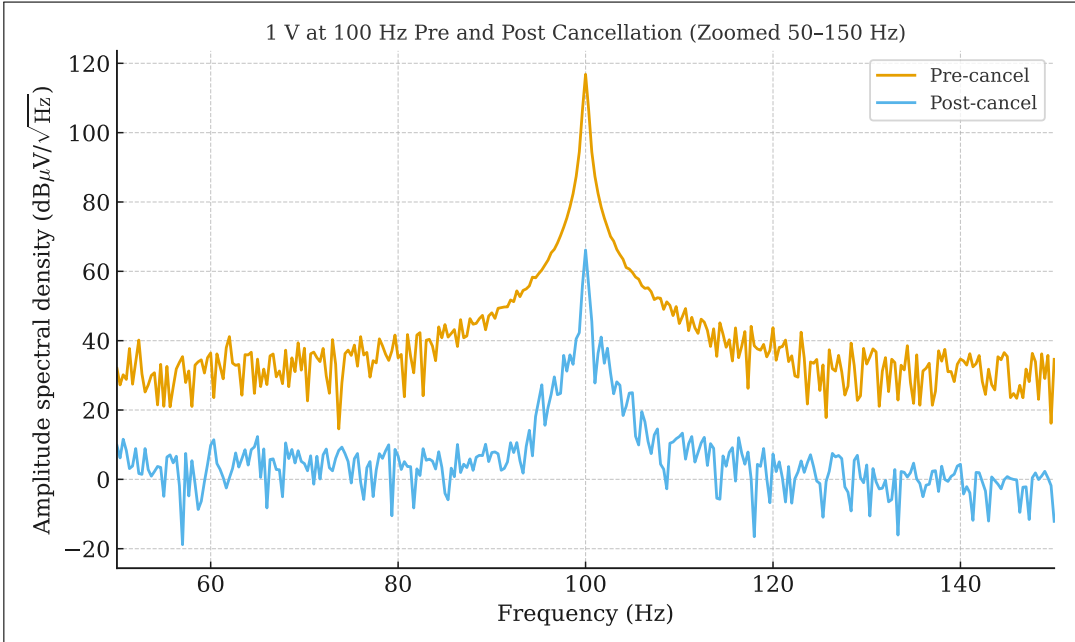


Figure 33: Residual spectra before and after analogue cancellation.

The limiting factors of an analogue implementation appear to be twofold⁷. First, the closed-loop path cannot achieve perfect nulling because of the observability constraint discussed earlier; even with strong open-loop compensation a finite coherent error must remain to provide a useable reference, limiting the accuracy of the I and Q estimates and thereby setting a floor on suppression. Second, there is a simulation-limited trade-off in the baseband

⁶All dB differences in this report refer to voltage ratios.

⁷A further practical complication, which does not necessarily reduce peak suppression, is frequency dependence: the feedforward-path gain and phase compensation must be tuned for each target carrier, adding setup overhead.

low-pass filtering: increasing the time constant suppresses residual ripple but forces longer runs with finer time steps; beyond a point, the required resolution becomes computationally intractable. Conversely, keeping the time constant on the order of seconds, as in the present simulation, permits higher resolution but leaves residual ripple that bounds the measurable suppression. However, this is not merely a limitation of the simulation: in practice, time constants much longer than a few seconds are undesirable, since coherent tracking of the artefact requires responsiveness and excessive time constants introduce latency⁸. For these reasons, a digital implementation of the mechanism is pursued as a potential alternative.

Summary

- **Purpose:** validate feasibility and reveal control dynamics via LTspice before committing to hardware.
- **Architecture tested:** closed-loop path (band-pass → I/Q mix → low-pass → remodulate → subtract) plus a complementary feedforward branch (amplitude scale + phase trim) to deepen the null.
- **Gain regimes observed:** low gain = stable but shallow suppression (overdamped); high gain = runaway (unstable); mid gain = fast convergence yet incomplete null (stable underdamped).
- **Key insight:** the detector needs a coherent residual to guide adaptation; as the residual shrinks, estimates degrade –hence the role of the feedforward branch to optimise suppression depth while feedback maintains alignment.
- **Step tests:** phase and amplitude jumps are tracked with underdamped settling; I/Q states move to new equilibria as expected.
- **AGC detour resolved:** apparent amplitude–phase coupling traced to idealised mixer models; introducing realistic DC offsets removes the issue, making AGC unnecessary.
- **Performance limiters:** $\lesssim 60$ dB attenuation in simulation; sensitivity to baseband time constants (ripple vs latency/run time) and frequency-specific tuning of the feedforward path.
- **Takeaway:** analogue modelling proves the concept and clarifies control limits, but practical suppression depth and robustness are constrained –prompting exploration of an alternative realisation.

⁸For ordinary lock-in usage, very long time constants are valuable because the goal is to extract a tiny steady component at a fixed frequency, where latency is not a limiting factor.

6 Digital Implementation

This section presents the digital implementation of the cancellation loop, explains why it offers advantages over the analogue approach, and characterises its nulling performance.

6.1 Overview

Following the analogue simulations, the cancellation mechanism was implemented digitally to evaluate whether improved performance could be achieved. The full algorithm, developed in MATLAB and executed on a National Instruments data acquisition device (NI DAQ), is shown in Figure 34. The complete source code is provided in Adaptive Cancellation Script.

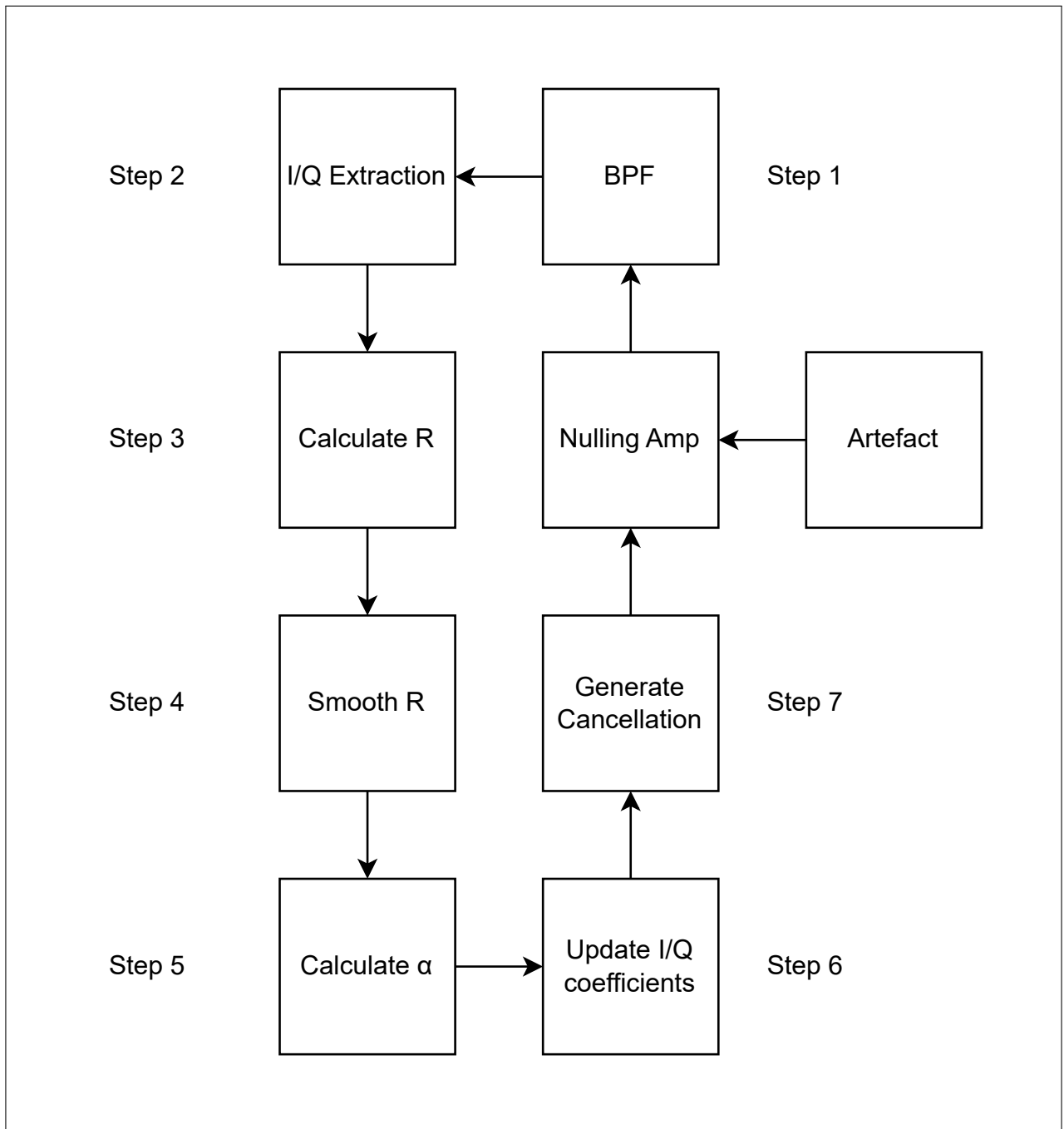


Figure 34: Algorithmic implementation of the artefact cancellation mechanism.

The algorithm proceeds as follows:

1. The acquired EEG signal $y[n]$ (digitised samples at time index n) is first passed through a digital band-pass filter centred at the stimulation frequency f_0 . This isolates the artefact carrier from off-band components.
2. In-phase and quadrature projections are computed by correlation with orthogonal reference sinusoids at frequency f_0 , evaluated over a window of N samples at times t_n :

$$I_{\text{meas}} = \frac{2}{N} \sum_{n=1}^N y[n] \cos(2\pi f_0 t_n), \quad Q_{\text{meas}} = \frac{2}{N} \sum_{n=1}^N y[n] \sin(2\pi f_0 t_n). \quad (25)$$

These yield slowly varying estimates of the artefact envelope.

3. The instantaneous residual amplitude is recovered as

$$R = \sqrt{I_{\text{meas}}^2 + Q_{\text{meas}}^2}. \quad (26)$$

4. To stabilise adaptation, R is smoothed by an exponential moving average:

$$R_{\text{smooth}} = (1 - \beta)R_{\text{smooth}} + \beta R, \quad (27)$$

where $\beta \ll 1$ is the smoothing constant.

5. The adaptive learning rate is then modulated according to the smoothed residual:

$$\alpha = \frac{\alpha_{\text{base}}}{1 + R_{\text{smooth}}}, \quad (28)$$

where α_{base} is the baseline step size. Large residuals accelerate convergence, while small residuals slow the update⁹.

6. The cancellation coefficients c_I, c_Q are updated using a least-mean-square (LMS)-like rule:

$$c_I \leftarrow (1 - \alpha)c_I - \alpha I_{\text{meas}}, \quad c_Q \leftarrow (1 - \alpha)c_Q - \alpha Q_{\text{meas}}. \quad (29)$$

7. Finally, the updated coefficients generate the cancellation signal:

$$x_{\text{cancellation}}[n] = c_I \cos(2\pi f_0 t_n) + c_Q \sin(2\pi f_0 t_n), \quad (30)$$

which is then scaled by a global gain:

$$x_{\text{cancellation,out}}[n] = \text{GAIN} \cdot x_{\text{cancellation}}[n]. \quad (31)$$

⁹Although the learning rate α decreases as R_{smooth} increases, the effective update in Step 6 grows with the residual (up to a cap), so large residuals produce larger corrections, whereas small residuals slow adaptation and gently pull the coefficients toward zero.

6.2 Performance

Unlike the analogue simulation, the digital implementation does not require an auxiliary feedforward path. The closed loop alone is sufficient, as the adaptive LMS update combined with exponential smoothing stabilises coefficient convergence even under very high loop gain. In principle, this allows the system to drive the cancellation tone down to the noise floor without losing observability, a limitation that forced the analogue loop to leave a finite pilot residual. The digital realisation is therefore expected to overcome the stability-suppression trade-off inherent to analogue control circuitry, offering deeper and more robust cancellation with a simpler architecture.

Figure 35 demonstrates the effectiveness of the digital closed-loop cancellation. The artefact is attenuated by approximately 100 dB, with the noise floor reduced by more than 40 dB. This represents a substantial improvement over the analogue simulation. It is important to note, however, that these results are merely instrumental. Validation requires assessing cancellation performance *in vivo*.

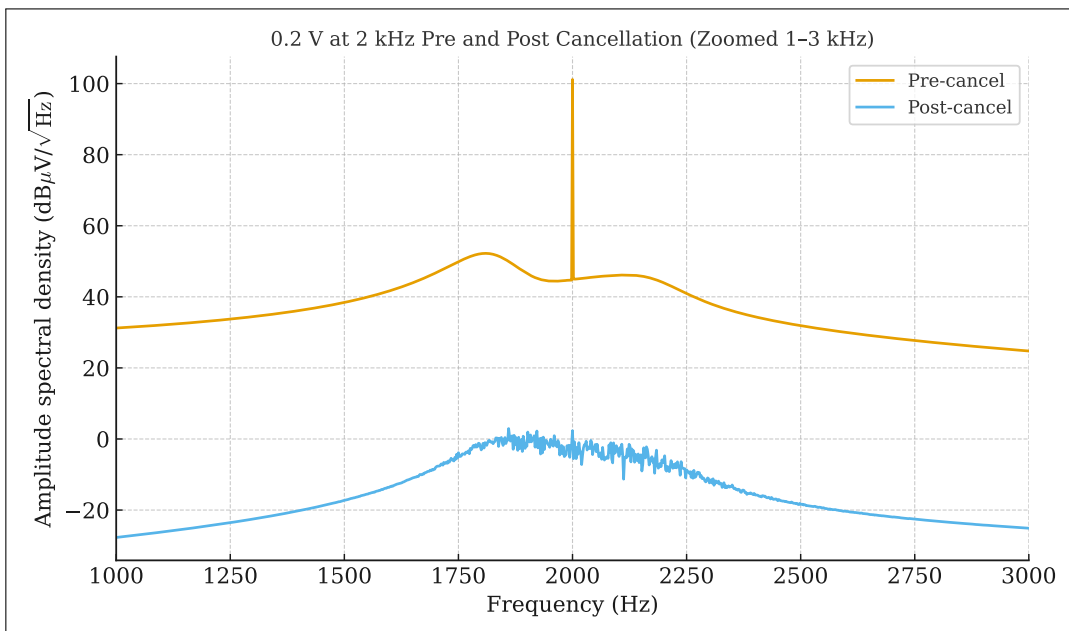


Figure 35: Residual spectra before and after digital cancellation.

Summary

- **Purpose:** implement the coherent cancellation mechanism in software to gain depth, stability, and ease of tuning.
- **Platform/architecture:** MATLAB + NI DAQ. Band-pass → coherent I/Q correlation → exponential moving-average smoothing (digital low-pass) → remodulate & subtract; plus residual-weighted LMS updates for fast, stable convergence.
- **Why it improves on analogue:** closed-loop only (no feedforward path required); high effective loop gain without runaway due to smoothing and step-size scheduling; straightforward parameterisation and portability across carriers/channels.
- **Performance:** instrumentation tests show ~ 100 dB carrier attenuation with >40 dB noise-floor reduction.
- **Caveat:** figures above are instrumental; *in vivo* effectiveness is assessed separately.
- **Takeaway:** resolves the stability-depth trade-off seen in analogue control systems and provides a robust basis for live experiments and scaling.

7 Experimentation

This section evaluates the cancellation mechanism *in vivo*. It first rules out instrumental IMD products, then describes the *in vivo* stimulation–recording arrangement. An eyes-open/eyes-closed contrast confirms identification of cortical alpha. Carrier suppression at 2 kHz is then quantified by comparing pre- and post-cancellation spectra. The recordings are also checked for low-frequency (≈ 2 Hz) transients associated with the NI DAQ update mechanism (“update clicks”). Finally, post-cancellation spectra around the carrier are profiled to examine components previously hidden beneath the phase-noise skirt.

7.1 Instrumental IMD Test

Before proceeding to *in vivo* trials, it is prudent to determine whether IMDs arise within the instrumentation itself. As discussed in the Background section, this distinction matters because any observed IM products may stem from front-end nonlinearity, genuine neural heterodyning, or other contributions. A controlled test case was constructed in which a 2 kHz stimulation tone of approximately 100 mV was injected together with an additional signal at 10 Hz of approximately 100 μ V. This arrangement directly tests whether IMDs arise in the EEG post-amplification chain rather than from neural activity. The recording, made post-cancellation using a high-performance actiCHamp EEG amplifier–DAQ (Brain Products GmbH), is shown in Figure 36 and Figure 37, highlighting the 2 kHz and 10 Hz regions, respectively. No IMDs are observed between the stimulation frequency and the additional injected signal¹⁰.

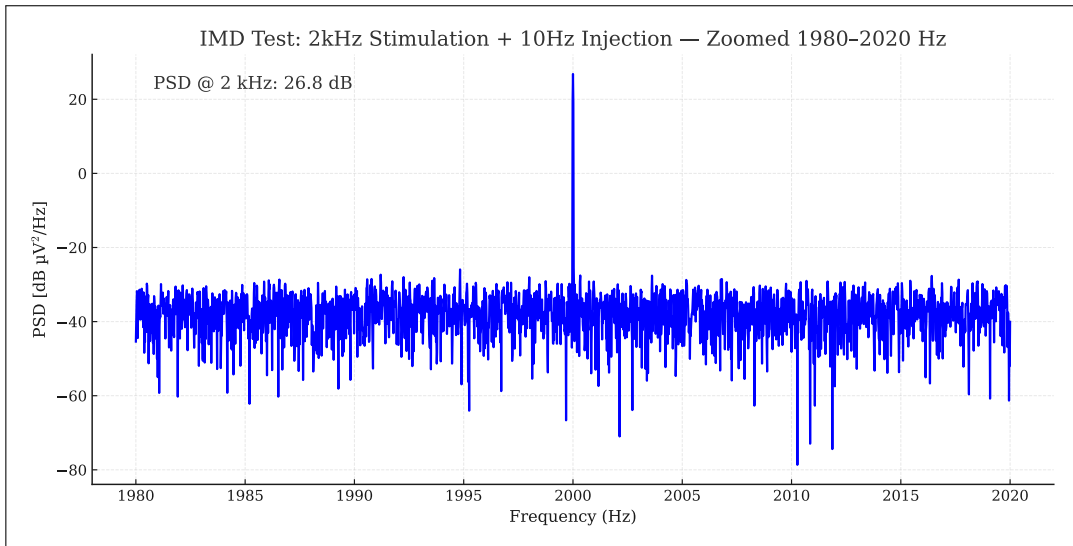


Figure 36: Power spectral density around the 2 kHz stimulation tone.

¹⁰Note that although PSDs are expressed in μ V²/Hz, in dB a halving of amplitude still corresponds to a 6 dB decrease (rather than 3 dB), since the PSD scales with squared voltage.

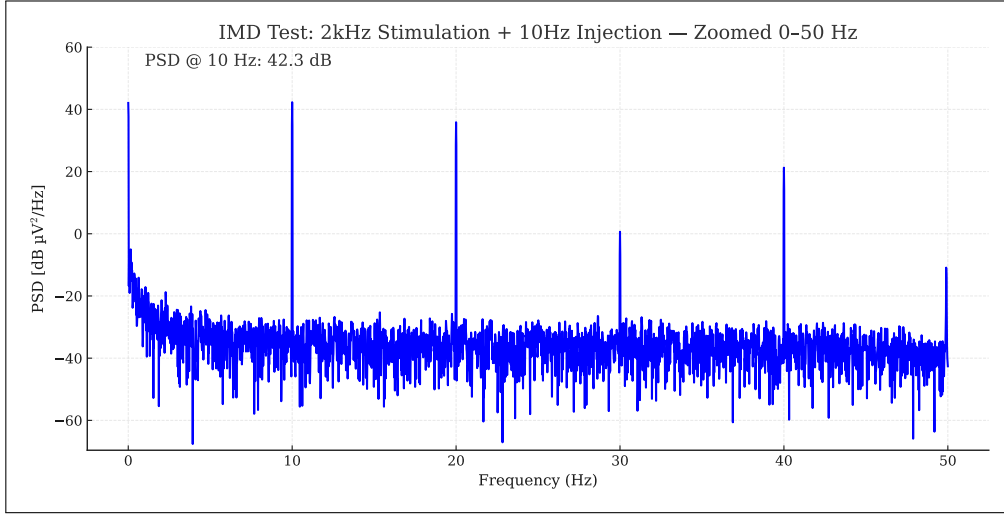


Figure 37: Power spectral density from 0 – 50 Hz validating the injected 10 Hz component.

7.2 In Vivo Setup

Figure 38 presents the *in vivo* setup. The NI DAQ synthesises a stimulation voltage, which a current stimulator (Linear Current Isolator, LCI; Soterix Medical Inc.) converts to differential current delivered via a bipolar stimulation electrode pair. Recording electrodes capture EEG containing the stimulation artefact and are fed to an EEG nulling amplifier, designed by a third party to AT's technical specifications; the amplifier residual is returned to the NI DAQ for closed-loop control. A second output of the same NI DAQ synthesises the controller's cancellation waveform. Before re-entering the nulling amplifier, this waveform passes through an SR560 preamplifier (Stanford Research Systems) configured as a high-pass filter to suppress low-frequency transients from the NI DAQ update steps. In parallel, signals are acquired with the actiCHamp to provide high dynamic range recordings. Recordings typically last three minutes, providing adequate spectral resolution for the pre- and post-cancellation analyses reported below.

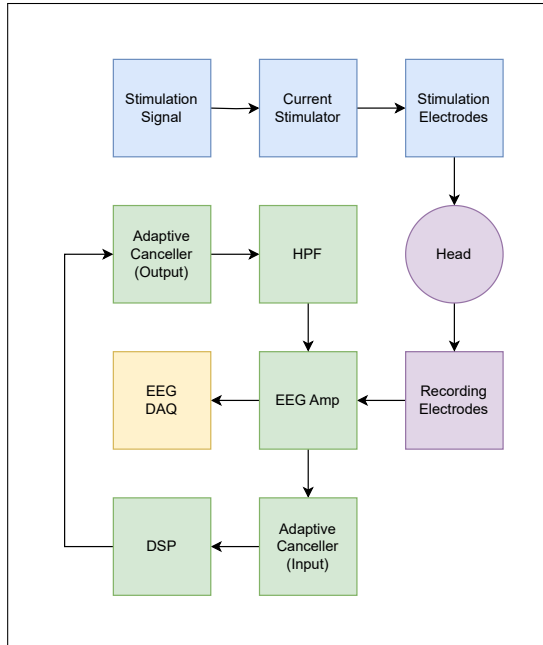


Figure 38: Block diagram of the experimentation setup.

7.3 Eyes Open vs. Eyes Closed Test

To verify that genuine cortical activity is observable with the stimulation hardware in place, an eyes-open versus eyes-closed contrast was acquired. The post-stimulus spectra, shown in Figure 39 and Figure 40, show the expected ~ 10 Hz alpha increase in the eyes-closed condition, confirming that neural signals are detected by the actiCHamp.

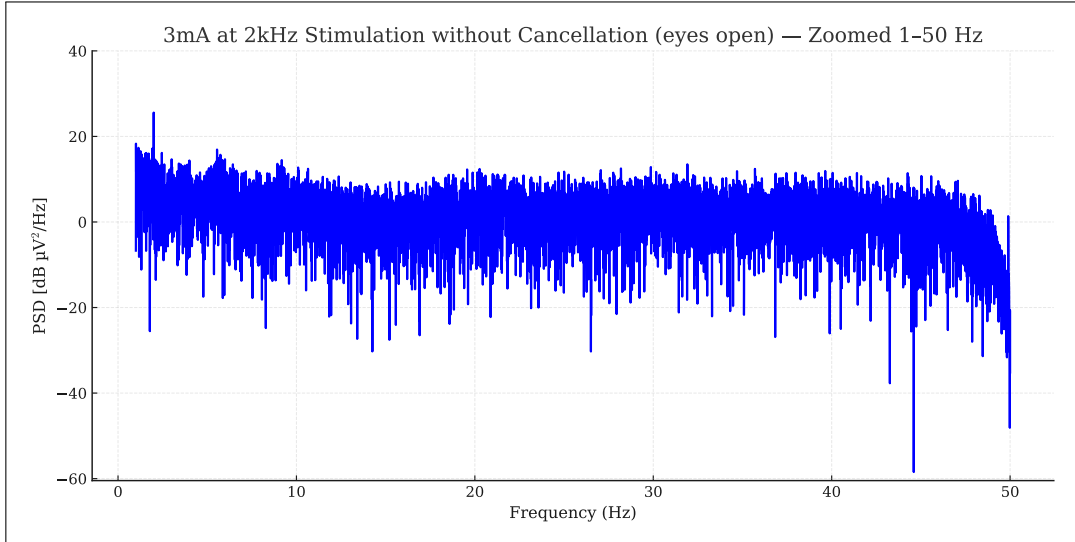


Figure 39: EEG spectrum with eyes open.

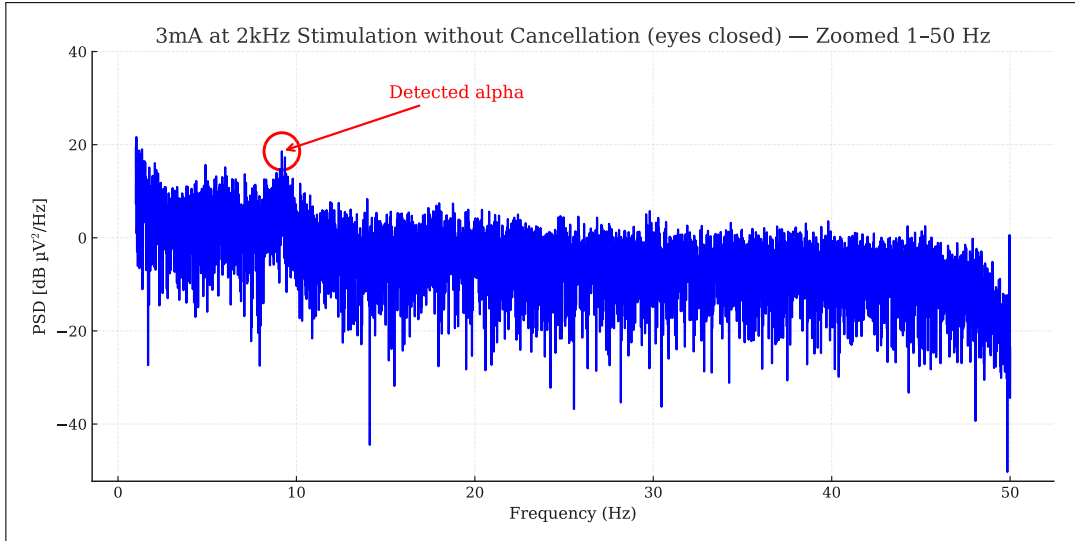


Figure 40: EEG spectrum with eyes closed, showing increased alpha activity near 10 Hz.

7.4 Pre- vs. Post-Cancellation

Having confirmed that neural signals can be recorded with the actiCHamp, the next step is to evaluate how effectively the cancellation mechanism suppresses the stimulation artefact. Figure 41 and Figure 42 compare spectra at 2 kHz under 3 mA transcranial alternating current stimulation (tACS)¹¹. Before cancellation, the artefact peak at the carrier is 113.1 dB μ V; after cancellation it is 30.4 dB μ V, corresponding to 82.7 dB suppression.

¹¹tACS is chosen since it is known to stimulate the visual cortex [19].

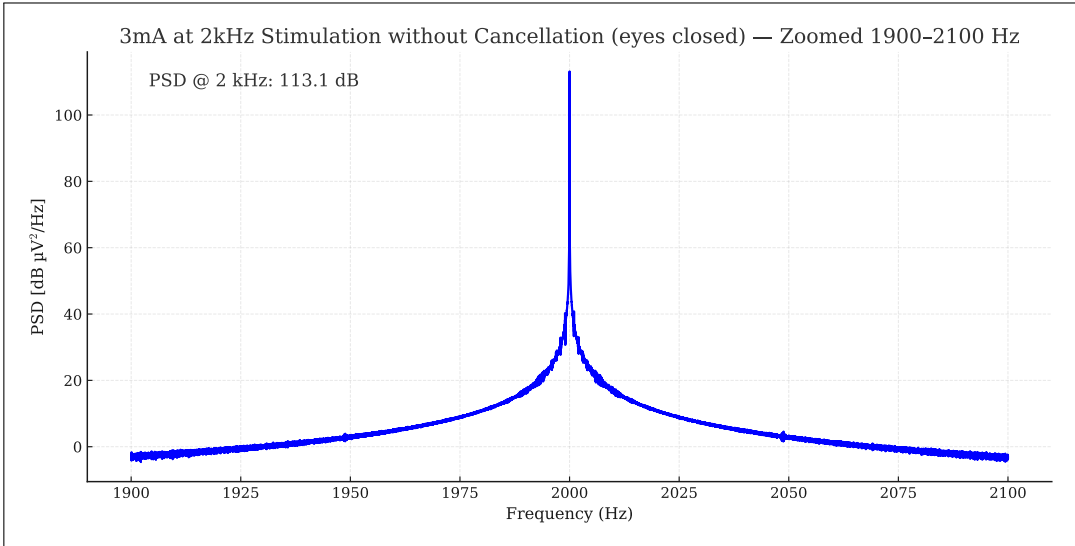


Figure 41: EEG spectrum with 3 mA stimulation before cancellation.

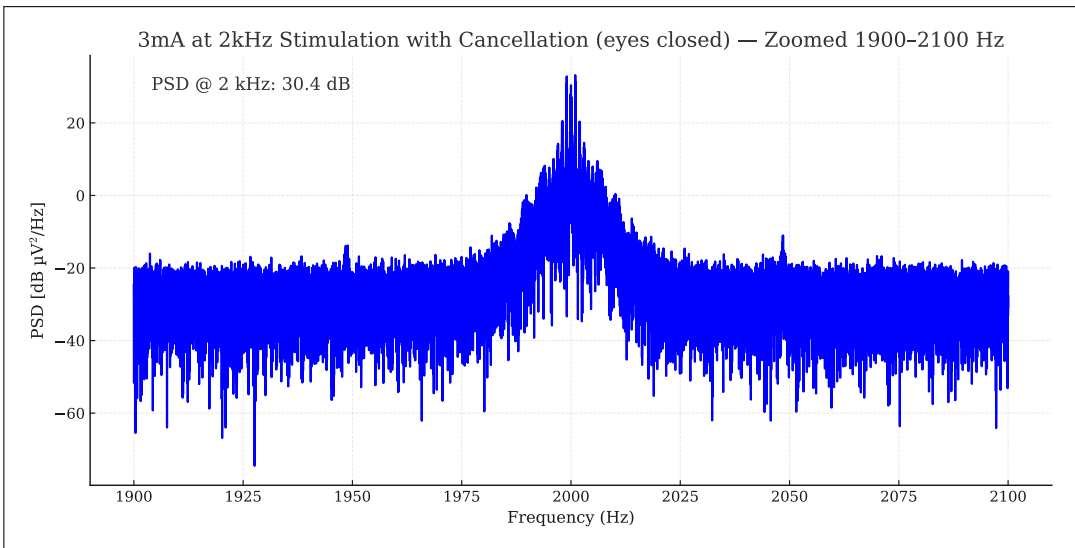


Figure 42: EEG spectrum with 3 mA stimulation after cancellation.

7.5 NI DAQ Update Clicks

Before examining the post-cancelled 2 kHz band in detail, it is important to confirm that the high-pass filtering has removed the 2 Hz transients generated by the NI DAQ¹². These artefacts arise because the system currently updates the cancellation signal using a buffered architecture rather than a direct digital synthesiser (DDS). A comparison of Figure 43 and Figure 44 shows no residual 2 Hz component in the post-cancellation recordings, indicating that such transients cannot produce hardware IMDs.

¹²Using the MATLAB API, the NI DAQ's fastest update period is 500 ms, corresponding to an update rate of 2 Hz.

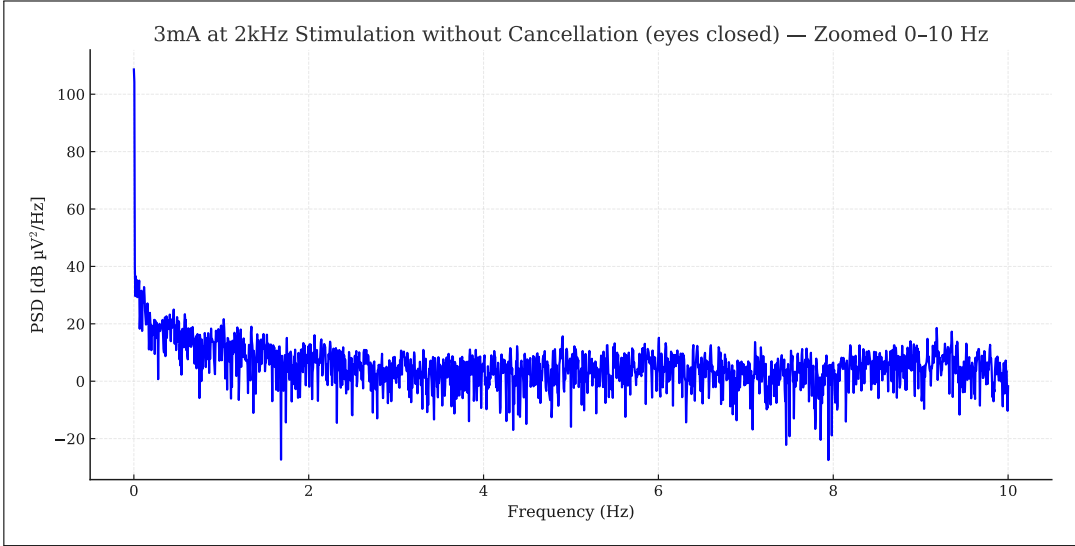


Figure 43: Pre-cancellation spectrum to test against post-cancellation spectrum.

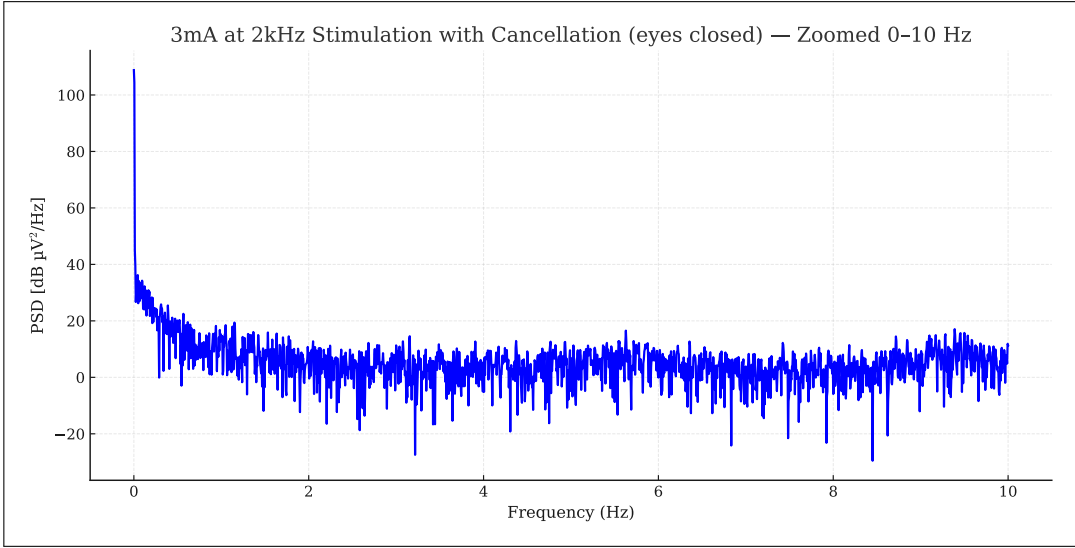


Figure 44: Post-cancellation spectrum showing absence of 2 Hz update artefacts.

7.6 Profiles of Post-Cancellation Recordings

With the DAQ-update artefacts removed by high-pass filtering, attention turns to the spectral region around the 2 kHz carrier after cancellation. Three representative recordings are shown in Figure 45, Figure 46, and Figure 47. A consistent pattern emerges: time-varying sidebands appear near 1–1.3 Hz together with harmonics, and more densely spaced components occur around 0.2–0.3 Hz. These features are compatible with physiological modulation reported during tACS [20]; however, in the absence of concurrent physiological measurements, a physiological origin cannot be concluded here. Irrespective of origin, these sidebands overlap the frequency region where neural heterodyning products would be expected and therefore complicate interpretation. In short, there is a roadblock: before addressing the fundamental question of whether neural heterodyning occurs non-invasively, the origin and insertion point of these nonlinear components must be established.

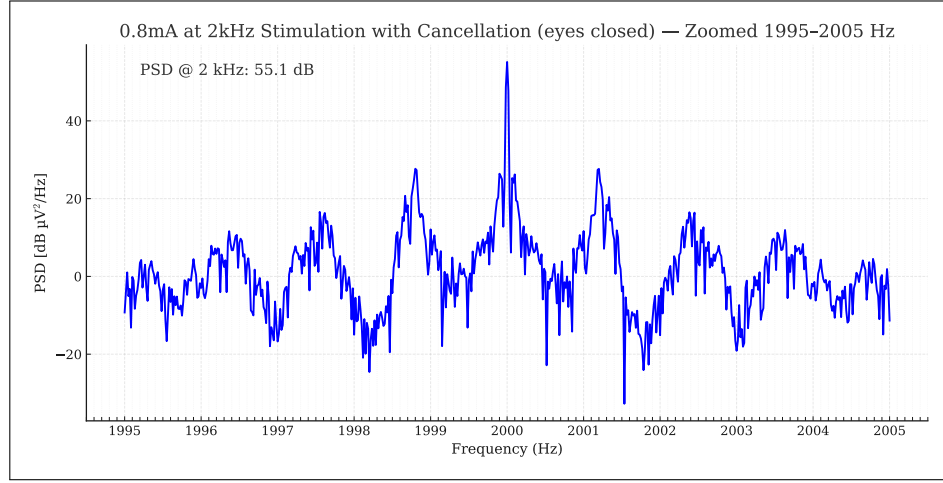


Figure 45: Post-cancellation spectrum at $800 \mu\text{A}$ stimulation, showing low-frequency sidebands around the 2 kHz carrier.

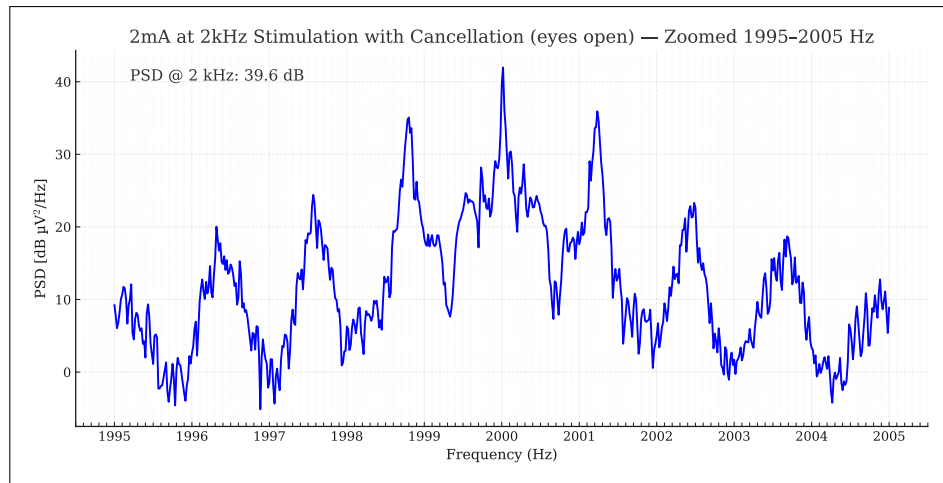


Figure 46: Post-cancellation spectrum at 2 mA stimulation, showing low-frequency sidebands around the 2 kHz carrier.

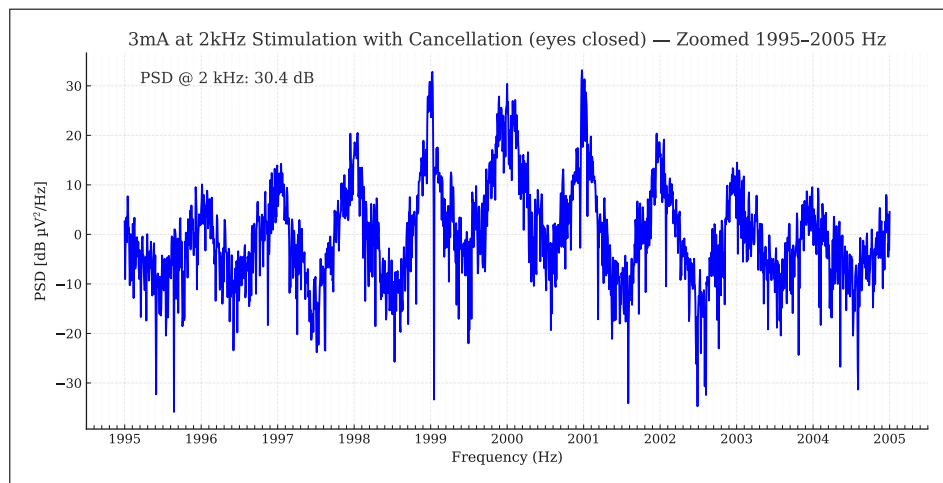


Figure 47: Post-cancellation spectrum at 3 mA stimulation, showing low-frequency sidebands around the 2 kHz carrier.

Summary

- **Aim:** assess coherent cancellation *in vivo* and analyse IM products near the carrier.
- **Instrumentation check:** with a 2 kHz tone and a 10 Hz injected control, post-cancellation recordings on actiCHamp show no IMD artefacts between them.
- **In vivo setup:** NI DAQ → current isolator for stimulation; EEG nulling amplifier in the loop; cancellation waveform returned via SR560 high-pass; parallel acquisition on actiCHamp; ~3-min segments for spectral resolution.
- **Physiology present:** eyes-closed vs eyes-open shows the expected alpha increase, confirming neural signal capture.
- **Carrier suppression:** at 3 mA tACS and 2 kHz, the carrier peak drops from 113.1 dB μ V to 30.4 dB μ V (82.7 dB attenuation).
- **Update artefacts:** NI DAQ 2 Hz “update clicks” are removed by high-pass conditioning; no residual line is observed.
- **Post-cancel landscape:** low-frequency sidebands persist around the carrier (notably ~0.2–0.3 Hz and ~1–1.3 Hz with harmonics); patterns and variability are compatible with physiological modulation.
- **Implication:** coherent cancellation works *in vivo*, but suspected physiological sidebands near the carrier currently mask any putative heterodyned neural components; pinpointing their origin becomes the next constraint to lift.

8 Further Applications

Although a roadblock remains for demonstrating neural heterodyning, the successfully implemented cancellation mechanism enables additional uses. In temporal interference (TI) stimulation, a prominent artefact arises at the difference frequency of the two drive tones. For example, driving at 2 kHz and 2.01 kHz produces a 10 Hz IMD component in the EEG recording, which must be characterised to separate neural from instrumental contributions. Because the present system can cancel one (or potentially both) carriers coherently, the difference-frequency IMD should be suppressed as well. An experiment was therefore conducted to test whether the same nulling amplifier and cancellation algorithm can eliminate the TI difference-frequency IMD.

8.1 TI In Vivo Setup

Figure 48 shows the *in vivo* arrangement for TI. The setup is identical to the tACS configuration except that an additional source–stimulator–electrode path delivers a second carrier (the position of the stimulation electrodes also differ). In the experiments, the 2 kHz tone was generated by the NI DAQ, while the 2.01 kHz tone was generated by an independent device (TiePie HS5). The cancellation algorithm and hardware were unchanged and targeted the NI DAQ tone. In other words, because the canceller’s LO is not frequency-locked to the TiePie carrier, only the 2 kHz component can be coherently nulled in this configuration.

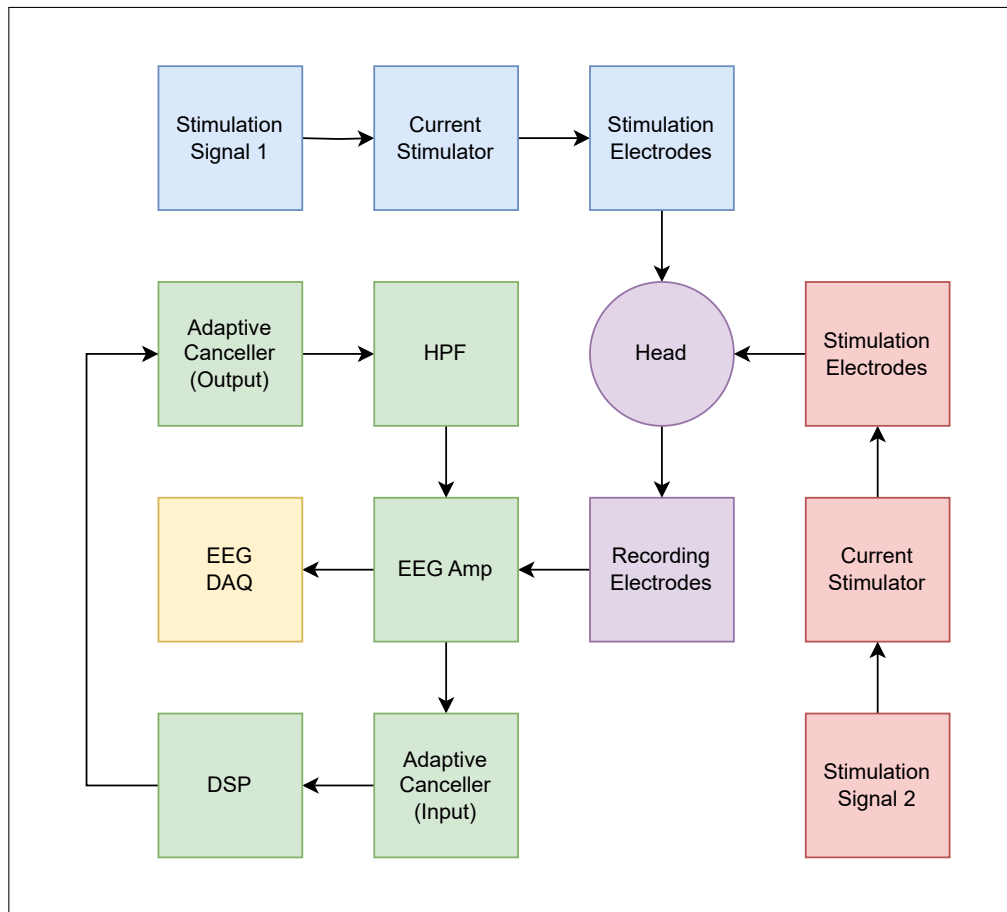


Figure 48: TI stimulation and recording arrangement.

8.2 Performance

Pre-cancellation spectra (Figure 49, Figure 50) show both TI carriers as artefacts and a 10 Hz IMD component at 24.7 dB_{PV}. Post-cancellation (Figure 51, Figure 52), the 2 kHz band is suppressed below the detection limit and the 10 Hz IMD is indistinguishable from the noise floor. This demonstrates that coherent removal of a single carrier is sufficient to eliminate the difference-frequency IMD in this setup.

These results, however, pertain to cancellation for a single electrode. For practical utility, artefacts must be suppressed across a full EEG array. A more effective approach, discussed with team members in Grossman Lab, is on-head cancellation, where a coherently synthesised anti-signal is injected near the reference or ground electrodes so that subtraction occurs on the head rather than inside the EEG nulling amplifier. This keeps the large carrier out of the front end, thereby minimising instrumental IMDs and extending suppression across the montage. Moreover, in clinical TI, the stimulation carriers are clocked independently of the canceller and are not frequency locked to it. Coherent suppression therefore requires establishing frequency and phase lock to the external carriers before enabling cancellation.

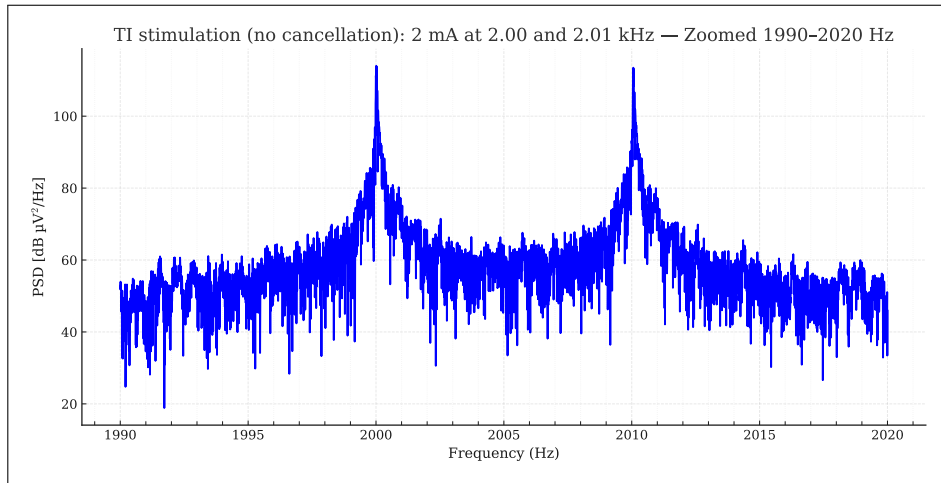


Figure 49: Pre-cancellation spectrum around 2 kHz with TI.

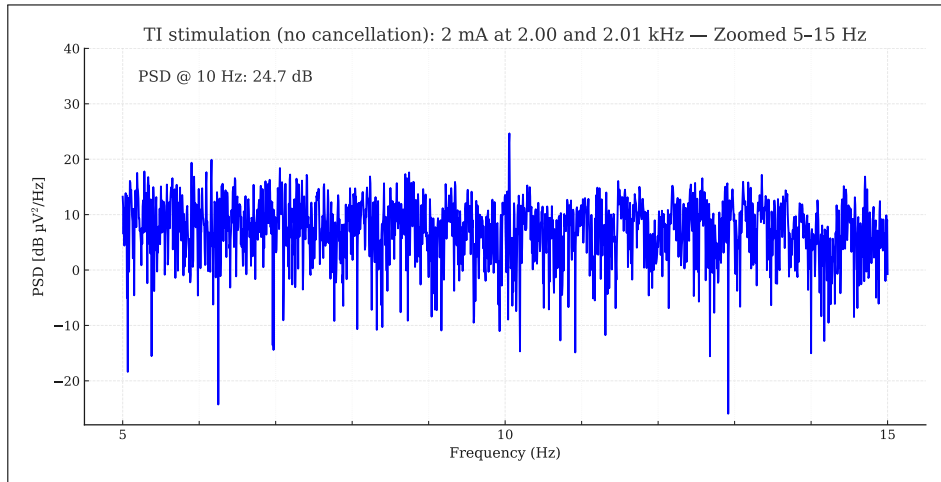


Figure 50: Pre-cancellation spectrum around 10 Hz showing the TI difference-frequency IMD.

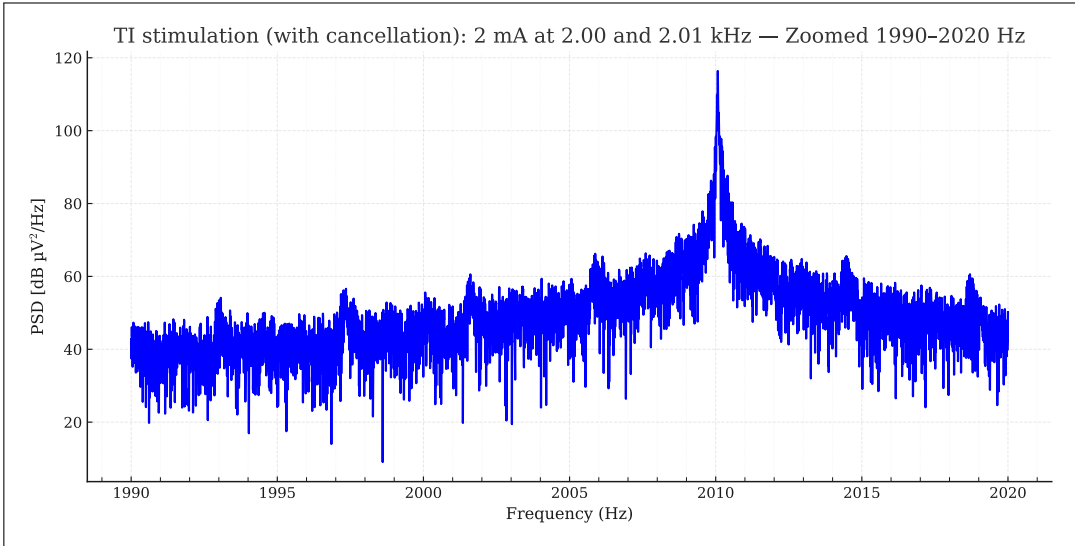


Figure 51: Post-cancellation spectrum around 2 kHz with the NI DAQ carrier nulled.

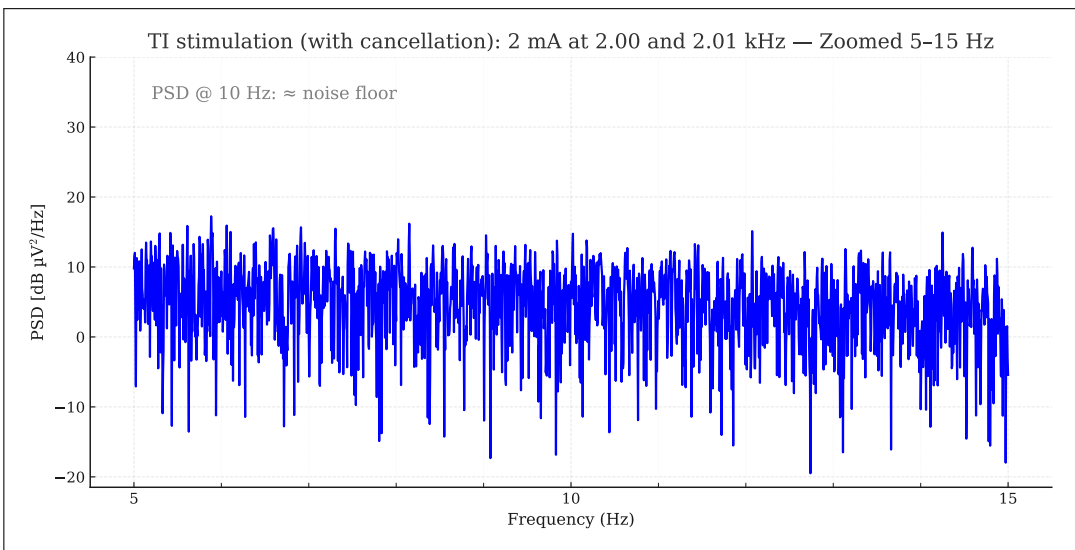


Figure 52: Post-cancellation spectrum around 10 Hz showing the removal of the difference-frequency IMD.

Summary

- **Aim:** test whether coherent cancellation aids TI by suppressing the difference-frequency artefact.
- **Setup:** two carriers at 2 kHz (NI DAQ) and 2.01 kHz (TiePie); canceller locked only to the NI DAQ carrier.
- **Result:** the 2 kHz carrier is driven below detection and the 10 Hz difference-frequency IMD collapses to the noise floor.
- **Interpretation:** coherent removal of a single TI carrier is sufficient to eliminate the difference-frequency artefact in this configuration.
- **Practical implication:** for montage-wide benefit, use on-head cancellation (inject anti-signal near reference/ground) to keep large carriers out of the EEG front end.
- **Clinical TI requirement:** Accept an external frequency/phase reference from third-party stimulators for compatibility with clinic workflows.
- **Next steps:** implement on-head cancellation, add robust external locking, and extend to multi-carrier/multi-channel operation.

9 Discussion

This section synthesises the report, advances conclusions that go beyond prior sections, and outlines current limitations together with future directions to transcend them.

9.1 Integrative Summary

The overarching rationale is to test whether endogenous rhythms can be shifted onto high-frequency carriers by neuronal non-linearities, enabling non-invasive, depth-resolved readout under kHz stimulation. Clinically, DBS is effective yet invasive, whereas TI offers a non-invasive route to deep targets. Invasive STN recordings during DBS exhibit spectral sidebands and strong time-domain correlations compatible with mixing, motivating a space-to-frequency encoding proposal in which multiple carriers tag distinct regions for scalp recovery. Translating this idea to EEG first encounters practical barriers: a dominant stimulation artefact with a close-in, time-correlated phase-noise skirt; ADC dynamic-range limits; and instrumental IM products that can mimic neuronal mixing. Consequently, establishing feasibility requires controlling the artefact before attempting a canonical non-invasive test of heterodyning.

The artefact analysis clarifies why naïve filters underperform. A narrow notch removes only the carrier line, leaving the skirt; a wide notch suppresses the skirt but also erases nearby components of interest. A simple signal model –clock jitter driving a numerically controlled source, followed by a slowly varying electrode–tissue path– explains the observed skirt as slow amplitude/phase wander around the carrier. The task is therefore not to delete a single line but to track and cancel a time-varying complex tone while preserving nearby content; this motivates carrier-referenced cancellation.

The mechanism is presented through complementary lenses. In control terms, a VLL generalises a PLL by locking the complex envelope rather than only the phase. In signal-processing terms, band-pass confinement around the carrier feeds coherent I/Q demodulation; low-pass filtering yields slow envelope estimates; remodulation and subtraction produce coherent cancellation while maintaining adjacent content. Physically, the internal I and Q states adapt toward the artefact’s envelope; the idealised model also flags a potential observability caveat at extremely deep nulls, which helps frame the implementation results.

Analogue simulation in LTspice validates feasibility and reveals control dynamics. A closed loop (band-pass → I/Q mix → low-pass → remodulate → subtract) achieves tracking but, across gain regimes, is either stable yet shallow (overdamped), unstable (runaway), or fast and stable but still leaves a residual (underdamped). This behaviour highlights the detector’s reliance on a coherent residual for guidance and motivates a complementary feedforward branch (amplitude scaling and phase trim) to deepen the null once alignment is established. Phase- and amplitude-step tests show underdamped settling with I/Q states moving to new equilibria. An apparent amplitude–phase coupling was traced to idealised mixer models and resolved by introducing realistic DC offsets, rendering AGC add-ons unnecessary. Practical limits include attenuation below ∼60 dB, sensitivity to baseband time constants (ripple versus latency/runtime), and frequency-specific tuning.

A digital realisation in MATLAB on an NI DAQ mirrors the same architecture –band-pass, coherent I/Q correlation, digital low-pass smoothing, residual-weighted LMS-style coefficient updates, then remodulation and subtraction– and overcomes several analogue constraints. The closed loop no longer requires a feedforward branch: smoothing and step-size scheduling allow high effective loop gain without runaway and with straightforward parameterisation across carriers/channels. Instrumentation tests show ~ 100 dB carrier attenuation and > 40 dB noise-floor reduction, with the reminder that these figures are instrumental rather than *in vivo*.

In vivo experiments proceed with appropriate controls. A 2 kHz tone with a 10 Hz injected control shows no post-cancellation IMD in the actiCHamp chain, reducing concern about instrumentation-induced mixing. The recording setup (current-isolated stimulation, nulling amplifier in the loop, SR560 high-pass return, parallel actiCHamp acquisition) captures physiological signals, as confirmed by the expected eyes-closed alpha increase. At 3 mA tACS and 2 kHz, the carrier peak drops from 113.1 dB_{PV} to 30.4 dB_{PV} (82.7 dB attenuation), and 2 Hz DAQ update artefacts are removed by conditioning. Post-cancellation spectra around the carrier consistently show low-frequency sidebands (~ 0.2 – 0.3 Hz and ~ 1 – 1.3 Hz with harmonics) whose variability and spacing match physiological modulation under tACS; these components currently mask any putative heterodyned neural signals.

Beyond tACS, a two-carrier TI test (2 kHz NI DAQ and 2.01 kHz TiePie, with locking to the NI DAQ tone only) demonstrates that nulling a single carrier collapses the 10 Hz difference-frequency artefact to the noise floor. The immediate practical implication is that coherent cancellation can benefit TI-EEG, with montage-wide suppression best achieved by on-head cancellation to keep large carriers out of the front end, and with clinical deployment requiring external frequency/phase locking to third-party stimulators.

Taken together, these results establish coherent I/Q cancellation as a practical route to artefact control under kHz stimulation: analogue modelling clarifies the control landscape and constraints; the digital implementation attains deeper, more stable suppression with simpler tuning; and *in vivo* recordings confirm substantial carrier removal while revealing persistent, possibly physiological sidebands that presently limit access to any heterodyned neural content. The TI case indicates promising utility for artefact-minimised protocols regardless of a definitive non-invasive demonstration of neural heterodyning.

9.2 Further Conclusions

Although putative neural heterodyning is masked by low-frequency sidebands near the carrier, if these sidebands are ultimately shown to be physiological, that would imply carrier-assisted observability –content otherwise buried by the $1/f$ EEG background.

Experience with the digital loop also re-weights the initially posited constraints. Under the tested instrumentation, deep carrier suppression also results in a lowered noise floor and no problematic hardware IMDs (if the sidebands are proven to be of physiological origin), indicating that dynamic-range and IMD concerns were initially over-emphasised relative to artefact tracking and phase-noise skirt control.

9.3 Novelty and Positioning

Coherent, carrier-referenced cancellation has had limited articulation in neuroscience contexts while existing descriptions provide sparse performance characterisation [21]. The present contribution is distinctive in its end-to-end clarity: an explicit artefact model that combines oscillator phase noise with a slowly varying electrode–tissue path; mutually consistent control, signal-processing, and physical views; a digitally stabilised VLL with transparent tuning (band-pass focus, digital low-pass smoothing, residual-weighted coefficient updates); and quantified suppression under *in vivo* conditions.

One might ask why coherent cancellation is preferred over driven-right-leg (DRL) strategies. DRL is designed primarily for broadband common-mode suppression [22], is less effective in the kHz range [23], and is not amenable to digital optimisation. That said, the proposed on-head cancellation is a hybrid of coherent cancellation and DRL: it injects a phase-aligned anti-signal near the reference/ground, combining frequency-specific nulling with montage-wide common-mode reduction – a capability that would be truly novel in TI-EEG if realised and validated.

9.4 Limitations and Future Directions

Two immediate limitations constrain interpretation and deployment. First, low-frequency sidebands of unknown origin persist near the carrier and obscure any clean test of non-invasive heterodyning. Their origin and insertion point need localisation (electrode–tissue interface or biological effects?). Second, a 2 Hz update architecture precludes tight external frequency/phase locking, limiting readiness for artefact-free EEG recording for TI.

Planned steps address these constraints. Hardware migration to an embedded DDS/FPGA-class platform with high-rate, phase-coherent updates and higher-resolution ADC/DACs should expand dynamic range, reduce injected quantisation noise, and enable multi-carrier, multi-channel operation with external clock acceptance. On-head cancellation will be prototyped to keep large carriers out of the EEG front end and to extend suppression across the montage, with safety and regulatory checks. Finally, to determine whether the low-frequency sidebands arise at the electrode-tissue interface, targeted electrode experiments are scheduled.

10 Sustainability and Societal Impact

This work implemented a coherent, carrier-referenced cancellation algorithm using existing equipment from Grossman Labs; no bespoke hardware was built. The incremental footprint is therefore small, dominated by laptop compute and routine consumables.

10.1 Environmental footprint and sustainability

Reusing stimulators, DAQs, and amplifiers avoided new manufacturing and e-waste. Power demands are modest (mA-level stimulation; lightweight computation). Future migration to a DDS/FPGA-class embedded platform can further cut energy use.

10.2 Societal benefits and opportunities

Deep artefact suppression during tACS/TI could yield artefact-minimised EEG, improving interpretability and enabling closed-loop non-invasive neuromodulation. A software-centric approach lowers cost and aids adoption across sites; open, well-documented algorithms support reproducibility and method standardisation.

10.3 Risks, ethics, and mitigations

Human studies must follow institutional approvals and stimulation safety limits. The controller should enforce hard limits, watchdogs, and safe states so suppression does not mask faults or induce unsafe currents. Data handling should meet established privacy and consent requirements.

10.4 Future sustainability actions

Planned steps include migrating to a low-power embedded platform with external clock acceptance and adding a short “sustainability note” to hardware documentation (power budget, repairability, parts lifecycle) to encourage responsible deployment.

11 Conclusion

Coherent I/Q cancellation produces deep attenuation of the stimulation carrier and enables post-cancellation spectral analysis under *in vivo* conditions. With the 2 kHz tone suppressed by up to ~ 83 dB and DAQ update artefacts controlled, low-frequency sidebands consistent with physiological modulation still remain. As a result, the present data do not yet permit a definitive assessment of neural heterodyning. The TI experiment shows that nulling a single carrier eliminates the 10 Hz difference-frequency IMD, highlighting utility beyond tACS artefact control. Immediate priorities are to localise physiological contributions (electrode–tissue interface or biological heterodyning) through targeted controls, and to extend the architecture with on-head cancellation and external phase locking to clinical stimulators. Together these steps would enable artefact-minimised EEG recording during TI and help establish a pathway toward a canonical demonstration of neural heterodyning in NIBS.

References

- [1] A. L. Benabid, S. Chabardes, J. Mitrofanis, and P. Pollak, “Deep brain stimulation of the subthalamic nucleus for the treatment of parkinson’s disease,” *Lancet Neurol.*, vol. 8, no. 1, Jan. 2009.
- [2] D. T. Chan, X. L. Zhu, J. H. Yeung, V. C. Mok, E. Wong, C. Lau, R. Wong, C. Lau, and W. S. Poon, “Complications of deep brain stimulation: a collective review,” *Asian Journal of Surgery*, vol. 32, no. 4, Oct. 2009.
- [3] N. Grossman, D. Bono, N. Dedic, S. B. Kodandaramaiah, A. Rudenko, H. J. Suk, A. M. Cassara, E. Neufeld, N. Kuster, L. H. Tsai, A. Pascual-Leone, and E. S. Boyden, “Noninvasive deep brain stimulation via temporally interfering electric fields,” *Cell*, vol. 169, no. 6, Jun. 2017.
- [4] I. R. Violante, K. Alania, A. M. Cassarà, E. Neufeld, E. Acerbo, R. Carron, A. Williamson, D. L. Kurtin, E. Rhodes, A. Hampshire, N. Kuster, E. S. Boyden, A. Pascual-Leone, and N. Grossman, “Non-invasive temporal interference electrical stimulation of the human hippocampus,” *Nat. Neurosci.*, vol. 26, oct 2023.
- [5] A. M. Cassarà, T. H. Newton, K. Zhuang, S. J. Regel, P. Achermann, A. Pascual-Leone, N. Kuster, and E. Neufeld, “Recommendations for the safe application of temporal interference stimulation in the human brain part i: Principles of electrical neuromodulation and adverse effects,” *Bioelectromagnetics*, vol. 46, no. 2, Feb. 2025.
- [6] A. Wagle Shukla, M. Bange, and M. Muthuraman, “Patient, target, device, and program selection for DBS in parkinson’s disease: advancing toward precision care,” *npj Parkinson’s Disease*, vol. 11, Jul. 2025.
- [7] R. S. Eisinger, M. E. Urdaneta, K. D. Foote, M. S. Okun, and A. Gunduz, “Non-motor characterization of the basal ganglia: Evidence from human and non-human primate electrophysiology,” *Front. Neurosci.*, vol. 12, Jul. 2018.
- [8] C. E. Luff, R. Peach, E.-J. Mallas, E. Rhodes, F. Laumann, E. S. Boyden, D. J. Sharp, M. Barahona, and N. Grossman, “The neuron mixer and its impact on human brain dynamics,” *Cell Rep.*, vol. 43, no. 6, Jun. 2024.
- [9] R. Sarpeshkar, *Ultra low power bioelectronics*. Cambridge, England: Cambridge University Press, Feb. 2010.
- [10] D. M. Pozar, *Microwave engineering, international adaptation*, 4th ed. Nashville, TN: John Wiley & Sons, Feb. 2021.
- [11] C. Wiest, F. Torrecillos, A. Pogosyan, F. Baig, E. A. Pereira, F. Morgante, K. Ashkan, and H. Tan, “STN LFP recordings from awake patients with Parkinson’s (on and off meds) and during 130 Hz DBS,” MRC BNDU Data Sharing Platform, University of Oxford, 2022.
- [12] C. Wiest, S. He, B. Duchet, A. Pogosyan, M. Benjaber, T. Denison, H. Hasegawa, K. Ashkan, F. Baig, I. Bertaina, F. Morgante, E. A. Pereira, F. Torrecillos, and H. Tan, “Evoked resonant neural activity in

subthalamic local field potentials reflects basal ganglia network dynamics,” *Neurobiol. Dis.*, vol. 178, Mar. 2023.

- [13] P. Horowitz and W. Hill, *The art of electronics*, 3rd ed. Cambridge, England: Cambridge University Press, Mar. 2015.
- [14] R. P. Singla and S. K. Sharma, “Power amplifier- memory-less non linear modeling,” *Theory and Applications of Physical Science*, vol. 2, Dec. 2019.
- [15] A. Hajimiri, “Phase noise in oscillators,” Presentation slides, SMIRC Lab, Stanford University, 1998. [Online]. Available: <http://smirc.stanford.edu/papers/Orals98s-ali.pdf>
- [16] A. Hajimiri and T. H. Lee, “A general theory of phase noise in electrical oscillators,” *IEEE J. Solid-State Circuits*, vol. 33, no. 2, Feb. 1998.
- [17] D. Ham and A. Hajimiri, “Virtual damping and einstein relation in oscillators,” *IEEE J. Solid-State Circuits*, vol. 38, no. 3, Mar. 2003.
- [18] N. S. Bland, “A need for time-varying models to suppress artefacts of tACS in the M/EEG,” *bioRxiv*, Jun. 2021.
- [19] Q. He, X.-Y. Yang, B. Gong, K. Bi, and F. Fang, “Boosting visual perceptual learning by transcranial alternating current stimulation over the visual cortex at alpha frequency,” *Brain Stimulation*, vol. 15, no. 3, 2022.
- [20] N. Noury, J. F. Hipp, and M. Siegel, “Physiological processes non-linearly affect electrophysiological recordings during transcranial electric stimulation,” *NeuroImage*, vol. 140, Oct. 2016.
- [21] S. Kohli and A. J. Casson, “Removal of gross artifacts of transcranial alternating current stimulation in simultaneous eeg monitoring,” *Sensors (Basel)*, vol. 19, no. 1, p. 190, 2019. [Online]. Available: <https://pubmed.ncbi.nlm.nih.gov/30621077/>
- [22] B. B. Winter and J. G. Webster, “Driven-right-leg circuit design,” *IEEE Transactions on Biomedical Engineering*, vol. BME-30, no. 1, pp. 62–66, 1983.
- [23] V. Acharya, “Improving common-mode rejection using the right-leg drive amplifier,” Texas Instruments, Application Report SBAA188, July 2011. [Online]. Available: <https://www.ti.com/lit/an/sbaa188/sbaa188.pdf>

A Adaptive Cancellation Script

```
1 %% =====
2 % ADAPTIVE CANCELLATION TEST (Single NI Device)
3 %
4 % What this script does (high level):
5 %   1) Opens a National Instruments DAQ session using the session-based API.
6 %   2) Generates a "stimulation" tone on A00 (e.g., an artifact/primary).
7 %   3) Optionally generates a "cancellation" tone on A01 to reduce the residual
8 %      measured on AIO via adaptive I/Q coefficient updates.
9 %   4) Runs continuously in the background with two callbacks:
10 %      - optimiser(event): processes incoming AI data, updates cancel I/Q.
11 %      - pushNext(src):    enqueues the next AO chunk (stim + cancel).
12 %   5) Ramps the stimulation amplitude up over a fixed duration to avoid
13 %      sudden steps. Cancellation is only allowed after the ramp (and if
14 %      enabled in cfg).
15 %   6) Plots time-domain signal, FFT, residual convergence, and I/Q history.
16 %   7) Optionally writes a one-time FFT CSV snapshot at a given time.
17 %
18 % Key ideas:
19 %   - I/Q demodulation at the test frequency to estimate residual amplitude.
20 %   - Simple gradient-like update of canc_I / canc_Q to cancel the residual.
21 %   - Gain/alpha scheduling based on smoothed residual magnitude.
22 %   - Saturation on AO1 to stay within safe DAQ output voltage limits.
23 %
24 % NOTE:
25 %   - This uses a single NI device ('Dev4'), so no hardware sync is needed.
26 %   - The session API is older; if using the "DataAcquisition" interface in
27 %     newer MATLAB releases, the code pattern differs.
28 % =====
29
30 %% === Setup DAQ Session =====
31
32 clearvars; clc; % Clean workspace and command window.
33
34 % --- Create a session with National Instruments hardware ---
35 s = daq.createSession('ni'); % Session-based DAQ (NI adaptor).
36
37 % --- Define devices and channels (SINGLE DEVICE) ---
38 % Channel map on Dev4 (as used by this script):
39 %   A00 = stimulation/primary tone (what creates the "artifact")
40 %   A01 = cancellation tone (what we adapt to null the residual)
41 %   AIO = residual input measurement (what we try to minimize)
42 devices = {
43     'Dev4', [0, 1], 'ao'; % Dev4 analog outputs: A00, A01
44     'Dev4', 0,       'ai'; % Dev4 analog input: AIO
```

```

45  };
46
47 % --- Add the specified channels to the session ---
48 for i = 1:size(devices,1)
49     dev    = devices{i,1};                      % Device name, e.g., 'Dev4'
50     chans = devices{i,2};                      % Channel index/indices
51     type   = devices{i,3};                      % 'ao' or 'ai'
52
53 if strcmp(type, 'ao')
54     % Add each analog output channel individually (Voltage mode)
55     for ch = chans
56         addAnalogOutputChannel(s, dev, ch, 'Voltage');
57     end
58 elseif strcmp(type, 'ai')
59     % Add analog input channel(s) (Voltage mode)
60     addAnalogInputChannel(s, dev, chans, 'Voltage');
61 end
62 end
63
64 % --- Configure session parameters ---
65 s.Rate = 250e3;                                % Samples/sec for both AI and AO
66 chunkSize = 125e3;                               % Samples per callback chunk (0.5 s)
67 s.IsContinuous = true;                           % Continuous background operation
68
69 % --- Hardware synchronization ---
70 % Not required because we are using a single NI device in one session.
71
72 %% ===== Global State Variables =====
73 % These are shared across the main script and the two callback functions.
74 % Using globals keeps the callbacks simple, but in production code you might
75 % encapsulate these in a handle class or a struct shared via UserData.
76
77 global Fs t_buffer canc_I canc_Q alpha_base gain R_smooth ...
78     h_td h_fft h_conv h_res h_iq history_R history_IQ ...
79     canc_plot_tone test_freq test_conditions current_test_index ...
80     last_state_change_time cancellation_frozen ...
81     ramp_done ramp_duration_sec ramp_samples_total ramp_samples_done ...
82     cancel_allowed
83 global snapshot_after_sec snapshot_written start_time run_label snapshot_dir
84
85 Fs = s.Rate;                                    % Sample rate (Hz), alias for convenience.
86 t_buffer = (0:chunkSize-1)' / Fs;               % Column time vector for one chunk.
87
88 % --- Adaptive cancellation state (I/Q coefficients and scheduling) ---
89 canc_I = 0;                                     % In-phase coefficient for A01 tone
90 canc_Q = 0;                                     % Quadrature coefficient for A01 tone
91 alpha_base = 0.05;                               % Base learning rate (will be scheduled)

```

```

92 gain = 30;                                % Scales the AO1 cancellation tone
93 R_smooth = 0;                               % Smoothed residual amplitude (for scheduling)
94 cancellation_frozen = false;                % If true, temporarily stop adapting
95
96 % --- Ramp management (controls when cancellation is allowed) ---
97 ramp_duration_sec = 10;                     % Desired ramp duration (s)
98 ramp_samples_total = round(ramp_duration_sec*Fs); % Total samples to ramp
99 ramp_samples_done = 0;                       % Samples elapsed in ramp
100 ramp_done = false;                         % True once full ramp reached
101 cancel_allowed = false;                    % True only if ramp_done & cfg.cancel
102
103 % --- Plot helpers / histories ---
104 canc_plot_tone = zeros(size(t_buffer));    % What AO1 is outputting (for display)
105 history_R = [];                           % Residual amplitude per update
106 history_IQ = [];                          % [I Q] per update
107
108 % --- Test condition(s) (tone frequency/amplitude and cancel enable) ---
109 % Multiple conditions could be cycled, but here we show one example record.
110 % For each struct:
111 %   f = [f_stim_Hz, f_unused]      (only the first is used here)
112 %   A = [A_stim_V, A_unused]       (only the first is used here)
113 %   cancel = logical              (true => allow cancellation after ramp)
114 test_conditions = {
115     struct('f', [2000, 2000], 'A', [10, 0], 'cancel', true)
116 };
117
118 current_test_index = 1;                   % Start from the first condition
119 last_state_change_time = tic;            % Timer for condition cycling
120 test_freq = test_conditions{1}.f(1);      % Demod frequency = stimulation freq
121
122 % --- FFT snapshot configuration (one-time CSV export of magnitude spectrum) ---
123 snapshot_after_sec = 40;                 % Take snapshot at t = 40 s (run time)
124 snapshot_written = false;                % Ensure only one snapshot per run
125 snapshot_dir = 'fft_exports';           % Output directory for CSV export
126 if ~exist(snapshot_dir, 'dir'); mkdir(snapshot_dir); end
127
128 %% ===== Initialize Plots =====
129 % Build axes + graphic handles up front so callbacks can update efficiently.
130
131 f_axis = linspace(0, Fs/2, chunkSize/2)'; % 1-sided FFT frequency axis (Hz)
132
133 figure;
134 h_td = plot(t_buffer, nan(chunkSize,1)); % Time-domain raw AI trace
135 title('Time-Domain Signal'); xlabel('Time (s)'); ylabel('V'); grid on;
136
137 figure;
138 h_fft = semilogx(f_axis, nan(chunkSize/2,1)); % 1-sided magnitude (dB)

```

```

139 title('FFT'); xlabel('Frequency (Hz)'); ylabel('dB'); grid on;
140 xlim([10 Fs/2]); % Start from 10 Hz for log axis clarity
141
142 figure;
143 h_conv = plot(nan, nan, '-ob'); % Convergence of |R| over iterations
144 title('Residual Amplitude'); xlabel('Iteration'); ylabel('|R|'); grid on;
145
146 figure;
147 h_res(1) = plot(t_buffer, nan(chunkSize,1), 'r'); hold on; % Input (AIO)
148 h_res(2) = plot(t_buffer, nan(chunkSize,1), 'g'); % AO1 cancel tone
149 legend('Input', 'Cancellation');
150 title('Signal and Cancellation'); xlabel('Time (s)'); ylabel('V'); grid on;
151
152 figure;
153 h_iq = plot(nan,nan,'-b', nan,nan,'-r'); % I and Q trajectories
154 legend('I', 'Q');
155 title('I/Q Coefficients'); xlabel('Iteration'); ylabel('Value'); grid on;
156
157 %% ===== Queue Initial Output =====
158 % We must always keep AO data queued ahead of the hardware. The pushNext()
159 % callback will keep feeding the pipeline after this initial queue.
160
161 cfg = test_conditions{1}; % Use the first (and only) test config.
162
163 % Label files (e.g., for FFT snapshot) based on whether cancellation is used.
164 if cfg.cancel
165     run_label = 'post_cancel';
166 else
167     run_label = 'pre_cancel';
168 end
169
170 % Generate the very first AO chunk using current I/Q (initially zero).
171 [ao0_stim, ao1_canc] = generateOutputs(cfg, t_buffer, canc_I, canc_Q, gain);
172 queueOutputData(s, [ao0_stim(:), ao1_canc(:)]); % Queue both AO channels
173
174 % Fire optimiser() once per chunk of AI data; ask for chunkSize samples.
175 s.NotifyWhenDataAvailableExceeds = chunkSize;
176
177 %% ===== Register Listeners (Callbacks) =====
178 % DataAvailable -> optimiser(event) : when AI buffer has chunkSize samples.
179 % DataRequired -> pushNext(src) : when AO needs more data for output.
180
181 s.addlistener('DataAvailable', @(src, event) optimiser(event));
182 s.addlistener('DataRequired', @(src, event) pushNext(src));
183
184 %% ===== Run =====
185 % Start background I/O and keep the UI responsive until the plots are closed.

```

```

186
187 disp('Starting cyclic adaptive cancellation test...');
188 fprintf('Ramp duration set to %.2f s. Cancellation will engage only after ramp and only if enabled in menu.\n',
189 → ramp_duration_sec);
190
191 start_time = tic; % Time reference for the snapshot
192 s.startBackground(); % Begin continuous AI/AO
193
194 % Keep MATLAB alive while the figures are open. Closing plots will end loop.
195 while isvalid(h_td)
196     pause(0.1); % Let callbacks and graphics run
197 end
198
199 % Clean shutdown: stop session and release hardware.
200 s.stop(); release(s);
201 disp('Finished.');
202
203 %% ===== Callback: Data Processing (Optimiser) =====
204 % This function is invoked whenever chunkSize AI samples are available.
205 % Responsibilities:
206 % - Filter the input around test_freq (narrow band).
207 % - Compute I/Q via weighted correlation (lock-in style).
208 % - Compute residual magnitude R and update canc_I/canc_Q (if allowed).
209 % - Freeze/unfreeze adaptation based on thresholds.
210 % - Update all plots and (optionally) write the FFT snapshot CSV.
211 function optimiser(ev)
212
213     global Fs t_buffer canc_I canc_Q alpha_base gain R_smooth ...
214         h_td h_fft h_conv h_res h_iq history_R history_IQ ...
215         canc_plot_tone test_freq cancellation_frozen cancel_allowed ...
216         snapshot_after_sec snapshot_written start_time run_label snapshot_dir
217
218     % == 1) Acquire raw data (one chunk): ==
219     ai_raw = ev.Data(:,1); % Read AIO from the event payload
220
221     % == 2) Band-pass filter around the known test frequency: ==
222     % Use a small, 6th-order IIR bandpass around [1999, 2001] Hz at Fs.
223     % This isolates the residual at test_freq and improves I/Q estimates.
224     persistent bpFilt
225     if isempty(bpFilt)
226         bpFilt = designfilt('bandpassiir', 'FilterOrder', 6, ...
227             'HalfPowerFrequency1', 1999, 'HalfPowerFrequency2', 2001, ...
228             'SampleRate', Fs);
229     end
230     ai_filt = filtfilt(bpFilt, ai_raw); % Zero-phase filtering (no lag)
231
232     % == 3) Build reference sinusoids at test_freq and a Hann window: ==
233     % Lock-in detection (I/Q): correlate filtered signal against cos/sin.

```

```

232     w      = hann(length(t_buffer));           % Window for robust estimates
233     refc = cos(2 * pi * test_freq * t_buffer); % In-phase reference
234     refs = sin(2 * pi * test_freq * t_buffer); % Quadrature reference
235
236     % === 4) Compute I/Q components via weighted inner products: ===
237     % The 2/sum(w) normalization makes these estimates scale-consistent.
238     I_meas = 2 / sum(w) * sum(w .* ai_filt .* refc);
239     Q_meas = 2 / sum(w) * sum(w .* ai_filt .* refs);
240     R      = hypot(I_meas, Q_meas);           % Residual amplitude magnitude
241
242     % === 5) Smooth residual for scheduling (slow EWMA): ===
243     R_smooth = (1 - 0.001) * R_smooth + (0.001 * R);
244
245     % === 6) Gain/alpha scheduling (very aggressive once residual appears): ===
246     % NOTE: These are heuristic knobs. The idea is to reduce alpha when
247     % residual is large (to avoid instability) and increase A01 gain.
248     if R_smooth > 1e-6
249         gain = 5e8;                         % Big gain to scale small canc_I/Q
250         alpha_base = 1e-9;                   % Very small base step size
251     end
252     alpha = alpha_base / (1 + R_smooth); % Decrease alpha as residual grows
253
254     % === 7) Adapt I/Q only if allowed (post-ramp AND cfg.cancel): ===
255     if cancel_allowed
256         % Gradient-like update: move canc_I/Q opposite to measured I/Q.
257         if R > 1e-6 && ~cancellation_frozen
258             canc_I = (1 - alpha) * canc_I - alpha * I_meas;
259             canc_Q = (1 - alpha) * canc_Q - alpha * Q_meas;
260         end
261
262         % Freeze when small; unfreeze if residual grows again (hysteresis).
263         if R < 1e-7 && ~cancellation_frozen
264             fprintf('>> Cancellation frozen (alpha = %.6e, R = %.6e)\n', alpha, R);
265             cancellation_frozen = true;
266         elseif R > 1e-3 && cancellation_frozen
267             fprintf('>> Cancellation unfrozen (alpha = %.6e, R = %.6e)\n', alpha, R);
268             cancellation_frozen = false;
269         end
270     end
271
272     % For traceability in the console/log:
273     fprintf('Residual amplitude R = %.6e\n', R);
274
275     % === 8) Update all plots with latest data: ===
276
277     % Time-domain traces:
278     set(h_td, 'YData', ai_raw);           % Raw AIO

```

```

279     set(h_res(1), 'YData', ai_raw);           % Input trace
280     set(h_res(2), 'YData', canc_plot_tone); % A01 tone (what we output)
281
282     % FFT magnitude (in dB) of filtered signal (display range is 1-sided):
283     Ya = abs(fft(ai_filt)); Ya = Ya(1:end/2);
284     set(h_fft, 'YData', 20*log10(Ya + eps)); % Avoid log(0) via eps
285
286     % Convergence plot: append residual magnitude
287     history_R(end+1) = R;
288     set(h_conv, 'XData', 1:numel(history_R), 'YData', history_R);
289
290     % I/Q history: append and update
291     history_IQ(end+1, :) = [canc_I, canc_Q];
292     set(h_iq(1), 'XData', 1:size(history_IQ,1), 'YData', history_IQ(:,1));
293     set(h_iq(2), 'XData', 1:size(history_IQ,1), 'YData', history_IQ(:,2));
294
295     % === 9) One-time FFT CSV snapshot at a fixed elapsed time: ===
296     if ~snapshot_written && toc(start_time) >= snapshot_after_sec
297
298         N = numel(ai_filt);
299         freqs = (0:(floor(N/2)-1))' * (Fs / N); % 1-sided frequency bins
300         mag_dB = 20*log10(Ya + eps);             % Magnitude in dB
301
302         T = table(freqs, mag_dB, 'VariableNames', {'frequency_hz','magnitude_db'});
303         stamp = datestr(now, 'yyyymmdd_HHMMSS'); % Timestamp for filename
304         fname = fullfile(snapshot_dir, sprintf('fft_%s_%s.csv', run_label, stamp));
305
306         try
307             writetable(T, fname);
308             fprintf('">> Saved FFT snapshot to "%s" at t=%.1f s (run: %s)\n', fname, toc(start_time), run_label);
309             snapshot_written = true;                % Only save once
310         catch ME
311             warning('Failed to write FFT snapshot: %s', ME.message);
312         end
313     end
314
315     drawnow limitrate;                      % Keep plots responsive without overloading
316
317 %% ===== Callback: Output Generator (pushNext) =====
318 % This function is called whenever the A0 engine needs more data.
319 % Responsibilities:
320 % - (Optionally) change test condition after a very long time (disabled
321 %   here by the giant threshold).
322 % - Generate the next A0 chunk using the latest canc_I/canc_Q.
323 % - Track ramp progress; enable cancellation only after ramp completes.
324 % - Queue the newly generated output to keep the A0 FIFO filled.
325 function pushNext(src)

```

```

326 global canc_I canc_Q t_buffer gain canc_plot_tone ...
327         test_conditions current_test_index last_state_change_time test_freq ...
328         cancellation_frozen ramp_done ramp_duration_sec
329
330 % (Effectively disabled) condition cycling after an enormous timeout.
331 % If you intend to cycle conditions, reduce this threshold to something
332 % meaningful (e.g., seconds to next condition).
333 if toc(last_state_change_time) > 200000
334     current_test_index = mod(current_test_index, numel(test_conditions)) + 1;
335     cfg = test_conditions{current_test_index};
336     test_freq = cfg.f(1); % Keep demod in sync with stim
337     cancellation_frozen = false; % Unfreeze on condition change
338     last_state_change_time = tic;
339     fprintf('Test %d f=[%.1f, %.1f] Hz, A=[%.5f, %.5f], Cancel=%d\n', ...
340             current_test_index, cfg.f(1), cfg.f(2), cfg.A(1), cfg.A(2), cfg.cancel);
341 % ^ Note: The "" is a stray character in the original printf; it
342 % prints fine but you may replace with '-' if desired.
343 end
344
345 % Use current test condition to generate the next AO buffer:
346 cfg = test_conditions{current_test_index};
347 prev_ramp_done = ramp_done; % For edge detection / logging
348 [ao0_stim, ao1_canc] = generateOutputs(cfg, t_buffer, canc_I, canc_Q, gain);
349
350 % Log when the ramp completes, and whether cancellation is enabled by cfg.
351 if ~prev_ramp_done && ramp_done
352     if cfg.cancel
353         fprintf('>> Ramp finished (%.2f s). Cancellation ENABLED (menu=true).\n', ramp_duration_sec);
354     else
355         fprintf('>> Ramp finished (%.2f s). Cancellation remains DISABLED (menu=false).\n', ramp_duration_sec);
356     end
357 end
358
359 % For display: remember what tone we just generated on AO1.
360 canc_plot_tone = ao1_canc;
361
362 % Queue the next pair of AO channels to keep the output streaming.
363 src.queueOutputData([ao0_stim(:), ao1_canc(:)]);
364 end
365
366 %% === Helper: Generate Stimulation (AO0) + Cancellation (AO1) =====
367 % generateOutputs(cfg, t, canc_I, canc_Q, gain)
368 % Inputs:
369 %   cfg : struct with fields f (Hz), A (V), cancel (bool)
370 %   t : time vector for the current chunk (seconds)
371 %   canc_I : in-phase coefficient for cancellation
372 %   canc_Q : quadrature coefficient for cancellation

```

```

373 % gain : scalar to scale the cancellation tone
374 % Outputs:
375 % ao0_stim: stimulation waveform for A00 (scaled artifact)
376 % ao1_canc: cancellation waveform for A01 (saturated to +/- 2.3 V)
377 %
378 % Behavior:
379 % - Applies a linear ramp (spanning multiple chunks) to the stimulation
380 %   amplitude to avoid steps. Tracks ramp progress globally.
381 % - Enables cancellation only when (cfg.cancel == true) AND ramp is done.
382 % - Canc tone = canc_I*cos(2ft) + canc_Q*sin(2ft), scaled and saturated.
383 function [ao0_stim, ao1_canc] = generateOutputs(cfg, t, canc_I, canc_Q, gain)
384     global ramp_done ramp_samples_total ramp_samples_done cancel_allowed
385
386 % Unpack the primary stimulation parameters:
387 f1 = cfg.f(1); % Primary frequency (Hz)
388 A1 = cfg.A(1); % Primary amplitude (V) pre-scaling
389 N = numel(t); % Chunk length (samples)
390
391 % --- Linear ramp over the first ramp_samples_total samples: ---
392 % idx counts global sample index across chunks; ramp goes from 0 -> 1.
393 if ramp_samples_done < ramp_samples_total
394     idx = (1:N)' + ramp_samples_done;
395     ramp = min(1, idx / ramp_samples_total);
396 else
397     ramp = ones(N,1); % Ramp complete => constant 1
398 end
399
400 % Update global ramp counters/state for subsequent chunks:
401 ramp_samples_done = min(ramp_samples_done + N, ramp_samples_total);
402 ramp_done = (ramp_samples_done >= ramp_samples_total);
403
404 % Determine if cancellation is permitted for THIS chunk:
405 cancel_allowed = (cfg.cancel && ramp_done);
406
407 % --- Stimulation (A00): the "artifact" we will try to cancel on AIO ---
408 artefact = ramp .* (A1 * sin(2 * pi * f1 * t)); % Primary tone with ramp
409 ao0_stim = 0.3 * artefact; % Scale down to safe volts
410 % TIP: The 0.3 factor adapts hardware-specific gains. Adjust as needed.
411
412 % --- Cancellation (A01): only emit once allowed (post-ramp & enabled) ---
413 if cancel_allowed
414     % Construct in-phase + quadrature cancellation at the same frequency.
415     canc_tone = canc_I * cos(2 * pi * f1 * t) + ...
416                 canc_Q * sin(2 * pi * f1 * t);
417 else
418     canc_tone = zeros(N,1); % No cancellation during ramp or if disabled
419 end

```

```
420
421      % Final AO1 signal with gain and saturation (protect hardware & safety):
422      ao1_canc = max(min(gain * canc_tone, 2.3), -2.3); % Clamp to +/- 2.3 V
423  end
424
```
